Materials Today • Volume xxx, Number xx • xxxx 2017 RESEARCH

ELSEVIER

Combining theory and experiment in lithium–sulfur batteries: Current progress and future perspectives

RESEARCH: Review

Xiang Chen [a], Tingzheng Hou [b,c], Kristin A. Persson [b,c,*], Qiang Zhang [a,*]

[a] Beijing Key Laboratory of Green Chemical Reaction Engineering and Technology, Department of Chemical Engineering, Tsinghua University, Beijing 100084, PR China
[b] Department of Materials Science and Engineering, University of California Berkeley, 210 Hearst Mining Building, Berkeley, CA 94704, United States
[c] Energy Technologies Area, Lawrence Berkeley National Laboratory, Berkeley, CA 94720, United States

Lithium–sulfur (Li–S) batteries are considered as promising candidates for next-generation energy storage devices due to their ultrahigh theoretical gravimetric energy density, cost-effectiveness, and environmental friendliness. However, the application of Li–S batteries remains challenging, mainly due to a lack of understanding of the complex chemical reactions and associated equilibria occurring in a working Li–S system. In this review, the typical applications of computational chemistry in Li–S battery studies, correlating to characterization techniques, such as X-ray diffraction, infra-red & Raman spectra, X-ray absorption spectroscopy, binding energy, and nuclear magnetic resonance, are reviewed. In particular, high-accuracy calculations and large-scale models, materials genome, and machine-learning approaches are expected to further advance computational design for the development of Li–S batteries and related fields.

1. Introduction

Advanced energy storage devices are playing an increasingly important role in modern society, including portable devices, electric vehicles, and large-scale smart grids [1–3]. Among various energy storage technologies, lithium-ion batteries (LIBs), which were launched in 1991 by Sony Corporation, currently outperform other systems and are dominating the battery market with a high market share of 63% worldwide [3–5]. However, the further applications of LIBs are hindered by the theoretical energy density limit (~400 Wh kg^{-1}), which is insufficient to supply the continuously increasing global energy demands [4,6,7]. Innovative battery systems beyond LIBs with high energy density are highly required.

Lithium–sulfur (Li–S) energy storage, which can deliver a high theoretical energy density of 2600 Wh kg^{-1}, has been considered as one of the most promising candidates for the next-generation energy storage devices [8–12]. The high energy density is achieved by utilizing the high-capacity sulfur cathode (1672 mA h g^{-1}) and lithium metal anode (3860 mA h g^{-1}), as well as the lowest negative electrochemical potential of the anode (−3.040 V *vs.* the standard hydrogen electrode). Furthermore, sulfur enjoys the advantages of abundant resources, low costs, and high biocompatibility, which are particularly attractive for reliable bulk energy storage applications [13–19].

The emergence of the Li–S battery is traced back to the 1960s, yet as compared to the rapid advancement of LIBs, it is still the incumbent technology [8,19]. The first long recyclable Li–S battery with nanocarbon/sulfur cathode was not demonstrated by Nazar and co-workers until 2009 [20], which announced the dawn of practical applications of Li–S batteries. An ordered nanostructured mesoporous carbon–sulfur hybrid cathode was demonstrated, achieving high, sustained, and reversible capacities. The improvement spurred further efforts devoted to Li–S batteries to promote their performance [21–28].

There have been many impactful and insightful reviews on Li–S batteries throughout the years, in which nanostructured sulfur cathodes [29–33], anodes [4,34–37], separators [38], and elec-

* Corresponding authors at: Beijing Key Laboratory of Green Chemical Reaction Engineering and Technology, Department of Chemical Engineering, Tsinghua University, Beijing 100084, PR China (Q. Zhang).
E-mail addresses: Persson, K.A. (kapersson@lbl.gov), Zhang, Q. (zhang-qiang@mails.tsinghua.edu.cn).

 https://doi.org/10.1016/j.mattod.2018.04.007

Please cite this article in press as: X. Chen et al., Materials Today, (2018), https://doi.org/10.1016/j.mattod.2018.04.007

trolytes [39–43] are well summarized from an experimental viewpoint. However, few of them provide a comprehensive introduction to the growing body of theoretical work aiding in the design of advanced Li–S batteries. The scope of this review is to provide an overview of the main directions and progress of the recent Li–S battery research from a theoretical viewpoint and to particularly demonstrate the significance of combining theory and experiment. A brief introduction to computational chemistry and materials design, including the most widely used theoretical methods, their applications in Li–S batteries, and the significance of combining theory and experiment, is also provided. The typical works in Li–S batteries that combine theory and experiment are summarized in terms of characterization techniques, including X-ray diffraction (XRD), infra-red (IR) & Raman spectra, X-ray absorption spectroscopy (XAS), binding energy, and nuclear magnetic resonance (NMR). The combination of theory and experiment and associated future challenges are discussed from the aspects of improved-accuracy calculations, large-scale models, materials genome, and machine-learning approaches. Finally, a short summary and perspective is provided at the end of this contribution.

2. Computational chemistry and materials design

Computational chemistry has become an important branch of modern science. Various methods have been developed [44], such as density functional theory (DFT), Hartree–Fock based models, the post-Hartree–Fock methods (configuration interaction, coupled cluster, the Møller–Plesset perturbation theory, *etc.*), molecular dynamics (MD), quantum mechanics/molecular mechanics (QM/MM), and other semi-empirical and empirical methods (Fig. 1). Among these methods, DFT, with a dramatic increase in the number of publications since 1990, has been widely employed in chemistry and materials science studies [45]. The core theorem of DFT states that the ground-state energy of a system is fully determined by its electron density distribution, as described by the Kohn–Sham equation [46].

Based on fundamental theoretical chemistry, computational chemistry has enjoyed a rapid development as a result of the exponential increase in computing power and access to robust software. Today, computational methods extend to almost every area of chemistry and materials science research. Scientists are able to perform *in silico* "experiments" (namely numerical simulations) and numerical simulations have become a trusted partner of experimental investigations. Occasionally, chemical simulations can provide the preferred method of choice when experiments cannot be implemented because of prohibitive conditions, convolution of phenomena, or other technical difficulties.

Recently, the ability to generate large amounts of systematic, simulated data has enabled the additional use of artificial

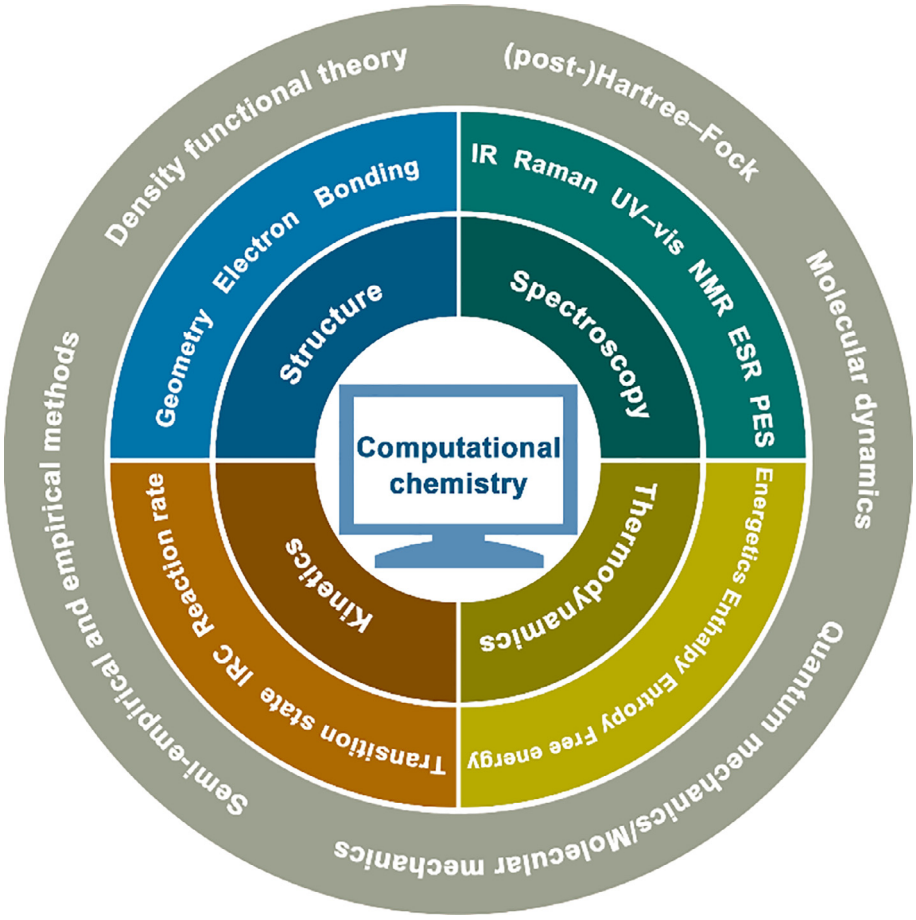

FIGURE 1

Schematic of typical methods and applications of computational chemistry.

Please cite this article in press as: X. Chen et al., Materials Today, (2018), https://doi.org/10.1016/j.mattod.2018.04.007

intelligence, especially machine learning, thus providing an emerging opportunity for computational chemistry applications [47]. For instance, Norquist and co-workers [48] used machine-learning algorithms trained on reaction data (failed or unsuccessful hydrothermal syntheses) to predict reaction outcomes, assisting the discovery of novel materials. Based on this method, the formation conditions for new organically templated inorganic products (vanadium selenite) were successfully predicted with a success rate of 89%, which exceeded the human intuition success rate of 78%. This example, as well as other works [49–52] that apply machine-learning techniques to chemical studies, demonstrates the power of computational approaches, particularly when it is combined with experimental verification.

Based the methods discussed above, here, we have divided the typical applications of computational chemistry for the study of Li–S batteries into four parts: structure, spectroscopy, thermodynamics, and kinetics (Fig. 1). A detailed introduction of these applications and corresponding examples are provided as follows:

(1) *Structure*: Geometrical and electronic structure optimization is one of the most basic applications of computational chemistry. To take this one step further, XRD, X-ray absorption fine structure (XAFS), extended X-ray absorption fine structure (EXAFS), molecular orbital (MO) energy level, orbital interaction (frontier analysis, fragment MO analysis, isolobal analogy, *etc.*), charge distribution, electrochemical potentials, and various bonding information can be acquired based on the optimized geometrical and electronic structures. For example, Hou et al. [53,54] optimized the structures of Li_2S_8 and N-doped nanocarbon materials and further investigated their interfacial interactions. The Bader charge, natural bond orbitals, and dipole analyses were conducted, based on which the interfacial interaction between Li_2S_8 and N-doped nanocarbon materials was described as an electrostatic dipole–dipole interaction, denoted a lithium bond. A rational design principle by proper doping of cathode materials was thus proposed.

(2) *Spectroscopy*: Various spectroscopies can be simulated computationally, such as IR spectroscopy, Raman spectroscopy, Ultraviolet–visible spectroscopy (UV–vis), NMR spectroscopy, electron spin resonance (ESR), and photoemission spectroscopy (PES) [including XAS and Ultraviolet photoelectron spectroscopy (UPS)]. For example, Ma et al. [55] calculated the IR spectra of (3-trimethoxysilylpropyl) diethylenetriamine (TMS-PDTA) and TMS-PDTA adsorbed with lithium polysulfides (LiPSs). An additional peak of 630 cm^{-1} of the Li–N stretch was found in LiPS-containing mixture, which agreed well with the experiments.

(3) *Thermodynamics*: Thermodynamic quantities, including energetics, enthalpy, entropy, and Gibbs' free energy, can be calculated by computational approaches in combination with statistical mechanics. Such basic properties are very important to assist in the understanding of the electrochemical reaction. For example, Assary et al. [56] calculated the energy, enthalpy, and Gibbs' free energy of various sulfur species, including sulfur molecules, lithium polysulfides, sulfur ions, and sulfur radicals. Accordingly, the energy, enthalpy, and Gibbs' free energy changes among these sulfur species conversions were determined, and the possibility of a specific conversion pathway was confirmed.

(4) *Kinetics*: It is very challenging and expensive to explore the reaction mechanisms and other kinetics only by experimental methods. However, both the transition states and intermediates of redox reactions in batteries can be studied through theoretical approaches. Therefore, both the reaction pathway and activation energy can be further inferred. Furthermore, the reaction process and the corresponding reaction products can be visually presented through MD simulations. Especially important for Li–S applications, the solvation chemistry (solvent effects, solvation structures, solvation energetics, *etc.*) can be better understood by theoretical approaches. For example, Chen et al. [57] investigated the decomposition of 1,3-dioxolane (DOL) and 1,2-dimethoxyethane (DME) electrolytes on Li metal surface. The reaction pathway was predicted through transition state calculations and further validated by *ab initio* molecular dynamics (AIMD) simulations.

The above four parts have summarized the typical applications of computational investigations in the Li–S battery studies. There are certainly more utilities that are not covered above, such as the calculation of optical (optical rotation, polarizability, hyperpolarizability, *etc.*), and magnetic properties (multiple moment, magnetic polarizability, magnetic coupling, *etc.*). While fundamental, these properties are out of scope of the current review and hence, we refer to other work for more details [58–60].

Due to the rapid rise of computer technology and the advancement of robust theoretical chemistry software, the power of computational chemistry is thriving. Larger systems and high-level methods are tractable and more factors can be taken into account than before. Computational chemistry is becoming an indispensable tool to help interpret experimental results, predict intrinsic properties, and investigate emerging chemical phenomena. Furthermore, *in silico* approaches are excellently poised to investigate highly radioactive, extremely explosive, or other hazardous materials, interstellar/circumstellar molecules in space, ultra-fast processes, and transient species (intermediates, transition states, excited states, *etc.*) or processes occurring under extreme conditions such as high temperature and pressure. Theoretical methods exhibit great advantages in these aspects, particularly in the cases of electronic structure analysis and exploration of reaction mechanisms. On the other hand, even with today's computing power, simulations are required to simplify real experimental conditions into model scenarios, frequently neglecting impurities, defects, and high-length scale effects. Therefore, combining calculations and experiments provides the best tradeoff to circumvent/complement their respective limitations and advantages.

However, care is necessary to ensure that computations and experimental controls and approximations are clearly defined and translated, to avoid seemingly contradictory results. Critical

Please cite this article in press as: X. Chen et al., Materials Today, (2018), https://doi.org/10.1016/j.mattod.2018.04.007

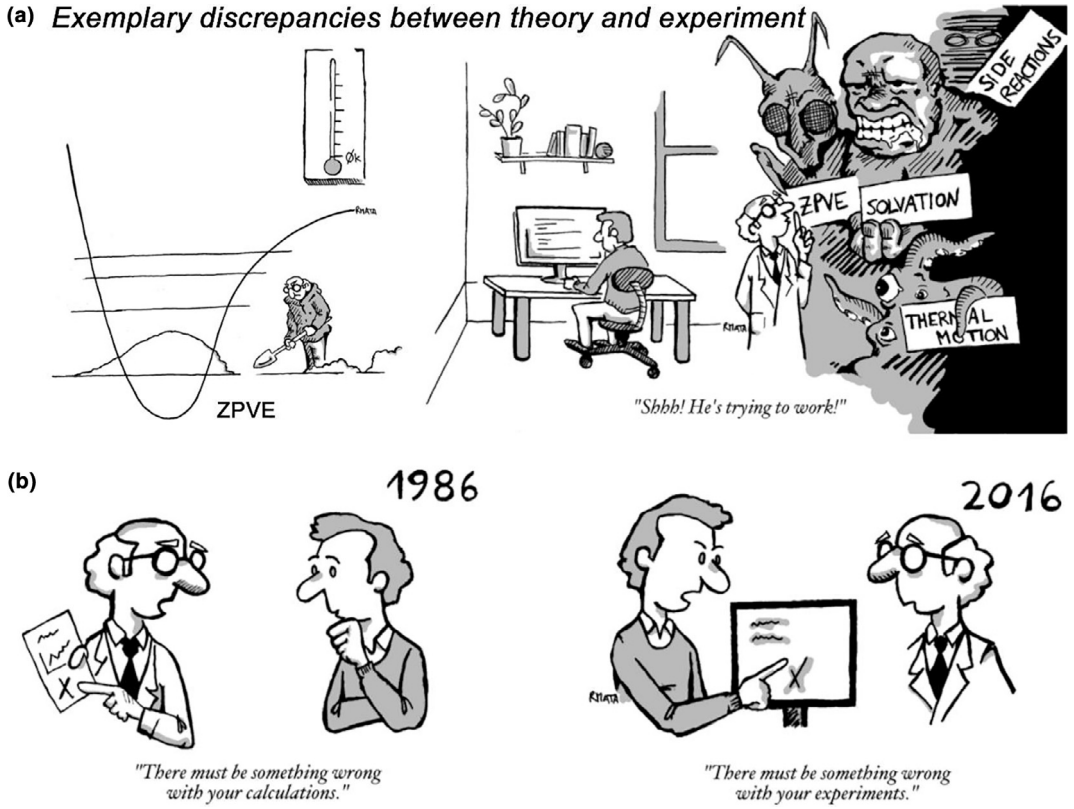

FIGURE 2

(a) Exemplary discrepancies between theory and experiments: ZPVE, solvation, side reactions, and thermal motion. (b) A false change of paradigm. Experience has taught us that one should be critical on both ends. (Reprinted with permission from [61]. 2017, Wiley.)

analysis, including effects which may cause discrepancy between the methodologies, such as zero-point vibrational energy (ZPVE), solvation effect, side reactions, and thermal motion, are imperative for a fruitful collaboration (Fig. 2). The key step to bridge the gap between theory and experiment is the efficient and appropriate modeling that can include all the essential factors and precisely abstract the nature of the object of study. In the following part, we provide examples on how to construct a model that captures the relevant complexities of the system, in order to elucidate Li–S energy storage mechanisms and operations.

3. The combination of theory and experiment

Generally, the practical application of Li–S batteries is currently impeded due to several obstacles, including (1) poor electrode rechargeability and limited rate capability owing to the insulating nature of sulfur and its reduction products (Li_2S and Li_2S_2), (2) rapid capacity attenuation resulting from the shuttle of soluble polysulfides, (3) growth of Li dendrites because of the uncontrollable Li deposition and unstable solid electrolyte interphase (SEI), and (4) rapid depletion of electrolyte due to irreversible side reactions during operation.

Recently, significant efforts have been devoted to overcoming the above issues and many advances have been made. Porous carbon [20,62–64], carbon nanotubes (CNTs) [65–68], graphene [69–78], (reduced) graphene oxides [79–82], conductive polymer [83,84], and their hybrids [85–93] have been adopted as the sulfur hosts in cathode, ameliorating the issues of low electrical conductivity and volume change to a large extent. Cui, Manthiram, Nazar, Zhang, and co-workers have reported rational design strategies of doped carbon [54,94–96], metal oxide [97–99], metal sulfide [98,100,101], and other hosts [98,99] for sulfur cathodes, which alleviates polysulfide shuttles and promotes the conversions among polysulfide intermediates. Furthermore, conductive nanostructured scaffolds construction [102–105], SEI modifications [106–111], solid-state electrolytes [112–114], and various electrolyte additives [115–117] have been explored to inhibit the growth of Li dendrites. In addition, the mechanism of electrolyte gassing and corresponding strategies have been well investigated [57,102,118,119].

Together with experimental explorations, calculations play an important part and afford a mechanistic and molecular insight into Li–S batteries [120–134], exhibiting advantages in the analyses of the physical and chemical properties of sulfur species (including the geometry, charge distribution, and spectroscopy), polysulfide–sulfur–host interaction (including binding energy and charge transfer), and reaction mechanisms. Mostly, the theoretical analyses are combined with experimental characterizations [53,55,101,135], such as XRD, IR & Raman spectroscopy, XAS, binding energy, and NMR, which are discussed individually in the following sections. A detailed introduction of corresponding key issues in Li–S batteries is first presented, followed by a detailed discussion of the combination of theory and experiment.

Please cite this article in press as: X. Chen et al., Materials Today, (2018), https://doi.org/10.1016/j.mattod.2018.04.007

3.1. XRD

The overall charge/discharge reaction occurring in Li–S batteries can be expressed as: $S_8 + 16Li \leftrightarrow 8Li_2S$ (rightward: discharge; leftward: charge). However, the detailed process of sulfur reduction is more complicated and involves many intermediates, such as Li_2S_8, Li_2S_6, Li_2S_4, and Li_2S_2, as well as various sulfur radicals. A universally accepted conversion and charge/discharge mechanism among these sulfur species is still lacking. Among the polysulfides, only sulfur, Li_2S_2, and Li_2S remain in their solid state in ether-based electrolytes. The existence of solid–liquid–solid triphase conversion reactions significantly increases the complexity. Notably, Li_2S_2 is the only solid-state intermediate in the charge/discharge process, and substantial efforts have been devoted to the study of Li_2S_2 to understand its structure, chemical and physical properties, as well as its role in the operation of Li–S batteries.

Amorphous lithium disulfide can be obtained directly via the universal sulfur reduction method using lithium triethylborohydride, however crystalline Li_2S_2 is more difficult to synthesize, in contrast to other alkaline disulfides, such as Na_2S_2 and K_2S_2 [136,137]. This is possibly caused by the much larger difference between the ionic radii of Li (76 pm) and S (184 pm) ions than that between Na (102 pm)/K (138 pm) and S ions [136,138]. To interrogate the properties of crystalline Li_2S_2, Kao [139], Wang [140], and Kawase [141] et al. optimized the structure of various (poly)sulfides, including Li_2S_2, in vacuum through first-principles calculations. Assary et al. [56] calculated the molecular clusters of Li_2S_2 in non-aqueous electrolytes. Zaghib and coworkers [142] conducted an evolutionary algorithm/DFT study to predict the atomic and electronic structures of Li_2S_2 crystal. Their results illustrate that Li_2S_2 is metastable and, eventually, decomposes into Li_2S, which may explain why a few observations of Li_2S_2 have been reported. Based on the calculated Li_2S_2 crystal structure, the simulated XRD patterns are coincident with their in situ XRD results collected from a working Li–S cell (Fig. 3A) [143]. The XRD peaks are observed near the end of the first charge and before the end of the second discharge, which exhibit great disparities from that of sulfur and Li_2S. Therefore, these peaks are unambiguously confirmed as the XRD signal of Li_2S_2. The predicted Li_2S_2 crystal is a triclinic structure of P-1 space group and the predicted lattice constants differ by only 3% with experimental results (Fig. 3A and B).

XRD is one of the most widely used experimental techniques to characterize the crystal structure, chemical composition, and physical properties of materials and thin films. The collected XRD results are compared with the standard PDF (Powder Diffraction File) database to identify the structures of the samples. Indeed, the construction of the standard PDF database, which is generated from the X-ray diffraction and simulated patterns, is an excellent example of productive theory and experiment collaboration. However, due to the difficulty of acquiring crystallized samples, exemplified in the case of Li_2S_2, experimental data may be lacking. In these circumstances, DFT offers an excellent route toward basic structure and XRD pattern generation, thus providing an effective reference to the experimental results. In return, validating the simulated XRD against experimental results provides a valuable test for the theoretical description of the system.

3.2. IR & Raman spectroscopy

Both IR and Raman techniques are commonly used for the investigation of sulfur and polysulfides. Generally, the characteristic Raman signals of polysulfides lie in the area between 400 and 500 cm^{-1} and below 250 cm^{-1}, which are donated to the S–S stretch vibration and bending/torsional modes, respectively [144]. However, the positions of the polysulfide Raman lines are highly dependent on solvent, temperature, and the kinds of polysulfide anion. They can vary several cm^{-1} even for the same polysulfide species [144,145]. Evidence suggests that several lithium polysulfides co-exist through complex chemical equilibria [24,39,146,147]. Furthermore, lithium polysulfides are readily oxidized to oxy-sulfur compounds due to disproportionation or side reactions [148], such as:

$$1/2S_8 + 4H_2O \rightleftharpoons 3HS + SO_4^{2-} + 5H^+$$

$$S_n^{2-} + 3/2O_2 \rightarrow S_2O_3^{2-} + (n-2)/S_8$$

These all add to the difficulty of synthesizing individual stoichiometric compounds for generating reference spectra. Even though single-crystal lithium polysulfide species can be obtained experimentally, the Raman spectra from the crystalline solids exhibit fundamental

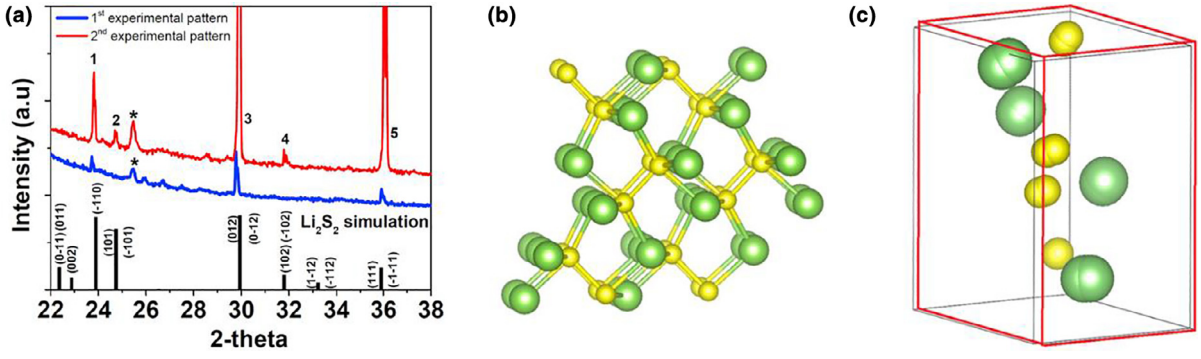

FIGURE 3

Combination of theory and experiment in XRD. (a) Comparison between the simulated (black lines) and the observed (red and blue lines) XRD patterns of Li_2S_2. (b) Li_2S_2 crystal structure (sulfur in yellow and lithium in green). (c) Schematic diagram showing the lattice parameter differences in fitted (thin black frame) and calculated (red frame) data. (Reprinted with permission from [143]. 2016, Elsevier.)

Please cite this article in press as: X. Chen et al., Materials Today, (2018), https://doi.org/10.1016/j.mattod.2018.04.007

differences as compared to solvated polysulfide anions in a working battery, as cations in the crystal lattice extort a vital influence on the solid-state spectra. The analyses of IR spectra from Li–S cells face similar challenges. All of these factors increase the difficulties in correctly analyzing the experimental IR and Raman results in a working Li–S cell.

In contrast, controlled simulations of IR and Raman spectra of single-sulfide species can be performed separately, and in different electrolyte environments, which can help deconvolute the collected experimental spectra. Chen and co-workers [140] conducted a quantum–chemical investigation on various polysulfides. Specifically, the IR and Raman frequencies of S_8 at B3LYP/6-311G (3df) level were obtained (Table 1), which agreed with the experimental data. This study demonstrates the reliability of theoretical IR and Raman spectra and their application in interpreting the spectra of complicated chemical systems. Kaskel and co-workers [144] calculated the Raman spectra of various polysulfide anions and radicals in tetrahydrofuran (THF) solvent through a similar method (Fig. 4A and B) and scrutinized the Raman assignments in comparison with experimental results (Table 2). The values provided in Table 2 can be used to interpret the measured spectra and afford a good overview concerning Raman measurements in Li–S batteries. An in situ Raman measurement of a Li–S cell during the overall discharge and charge processes was further performed (Fig. 4C and D). The experimental profiles were interpreted based on the calculation results and the characteristic peaks were identified. The conversion of sulfur species as a function of charge/discharge voltage was further unveiled based on this understanding. The typical S_8 peaks at 150, 220, and 470 cm^{-1} appear at the open-circuit voltage (OCV) of the discharge process but disappear almost completely after some time of potentiostatic discharge (2.33 V), indicating the reduction and depletion of sulfur. Two broad peaks emerge among 340–420 and 420–480 cm^{-1} between 2.29 V and the OCV voltage. The first peak was interpreted as resulting from a combination of S_6^{2-}, S_7^{2-}, and S_8^{2-} species, and the latter as S_3^{2-}, S_4^{2-}, S_5^{2-}, and S_4^{-}. A similar analysis was provided under different voltages during both the charge and discharge processes, thus providing a fresh insight into the charge/discharge mechanism.

Similarly, theoretical IR spectra in combination with experiments have been applied in the study of Li–S batteries, which help illustrate the bonding between polysulfides and the cathode host materials. Archer and co-workers [149] investigated the interaction between tethering polyethylenimine (PEI) polymers and LiPS (Fig. 5). The Li ion in LiPSs interacts with the N in the PEI host, forming a LiPS–PEI complex. Comparing with the original IR spectra of PEI, a new IR peak appears around 640 cm^{-1} in the complex, indicating the formation of a new chemical bond. Therefore, the new IR peak can be logically denoted to the as-formed Li—N bonds in the complex. The theoretical results are consistent with the experimental Fourier-transform IR (FTIR) results exhibiting a distinct but weak peak around 650 cm^{-1} in the spectrum of the LiPS/PEI mixture. Similar characterization techniques have also been applied to analyze the interaction between LiPSs and (3-trimethoxysilylpropyl)diethylenetriamine [55], 1-methy-3-trimethoxysilane imidazolium chloride [55], ethylenediamine-functionalized reduced graphene oxide [70], N-doped graphene [150], C_3N_4 [151], and TiO_2 [152].

TABLE 1

Calculated and observed IR and Raman frequencies of sulfur (cm^{-1}) at 30 K. R = Raman active, I = inactive, and Ir = infrared active. (Reprinted with permission from [140]· 2013, Elsevier.)

Calculated (S_8)		Experimental (α-sulfur)	
Frequency	**Designation**	**Frequency**	**Designation**
469.59		475	
213.97	R	218	R
375.63	I	411	I
241.40	Ir	243	Ir
460.85		471	
190.25	Ir	191	Ir
454.47		475	
144.38		152	
73.42	R	86	R
403.09		437	
248.45	R	248	R

3.3. XAS

The XAS is an element-specific technique while also sensitive to the local bonding chemistry and solvent environment [166]. Therefore, XAS can afford insights into the molecular structure and electronic charge state of various polysulfides in Li–S systems, and thus help understand the charge/discharge mechanism. However, it is difficult to interpret experimental S K-edge XAS data due to the lack of standards for polysulfides, similar to situation of IR & Raman spectra. Polysulfides disproportionate spontaneously in the electrolyte solution and establish an equilibrium of mixtures. Furthermore, fingerprinting using solid analogs can induce errors in the analysis as there is no guaranteed correspondence between the solid and solution phase XAS. The situation is even more challenging for polysulfide radicals in solution [167], as these are transient, highly reactive species.

Recently, DFT calculations have been applied to establish the standards for XAS interpretation. For example, Prendergast and co-workers [166,168,169] calculated the XAS spectra of a series of polysulfide molecules and radicals (Fig. 6A) and based on the simulations, proposed the origin of specific peaks in the XAS spectra. Considering the wide interest and the role of trisulfur radical in Li–S system [146,169–171], its detailed XAS spectrum analysis is highlighted in Fig. 6B. There are three main peaks in the spectrum: (1) a low-energy peak near 2468.5 eV arises from the $1s \rightarrow \pi^*$ transitions; (2) a broad, main feature near 2470.1 eV with σ^* character arises from transitions of the terminal sulfur atoms; (3) another broad peak near 2472.7 eV with σ^* character arises from transitions of the internal sulfur atom. This electronic-level insight into XAS spectra was compared to the in situ measured XAS data and resulted in a "best fit" (Fig. 6C and D). Exact weights of each sulfur component were therefore obtained from the fitting and the discharge mechanism was determined. Similar works have been carried out to probe polysulfide speciation and/or discharge/charge mechanism in Li–S batteries [170,172–178].

The theoretical analysis exhibits obvious advantages in complicated systems, such as the Li–S system. Experimentally collected spectrum can be difficult to interpret due to the complex chemical and electrochemical reactions and as-produced species in Li–S batteries. With an appropriate model, computational

Please cite this article in press as: X. Chen et al., Materials Today, (2018), https://doi.org/10.1016/j.mattod.2018.04.007

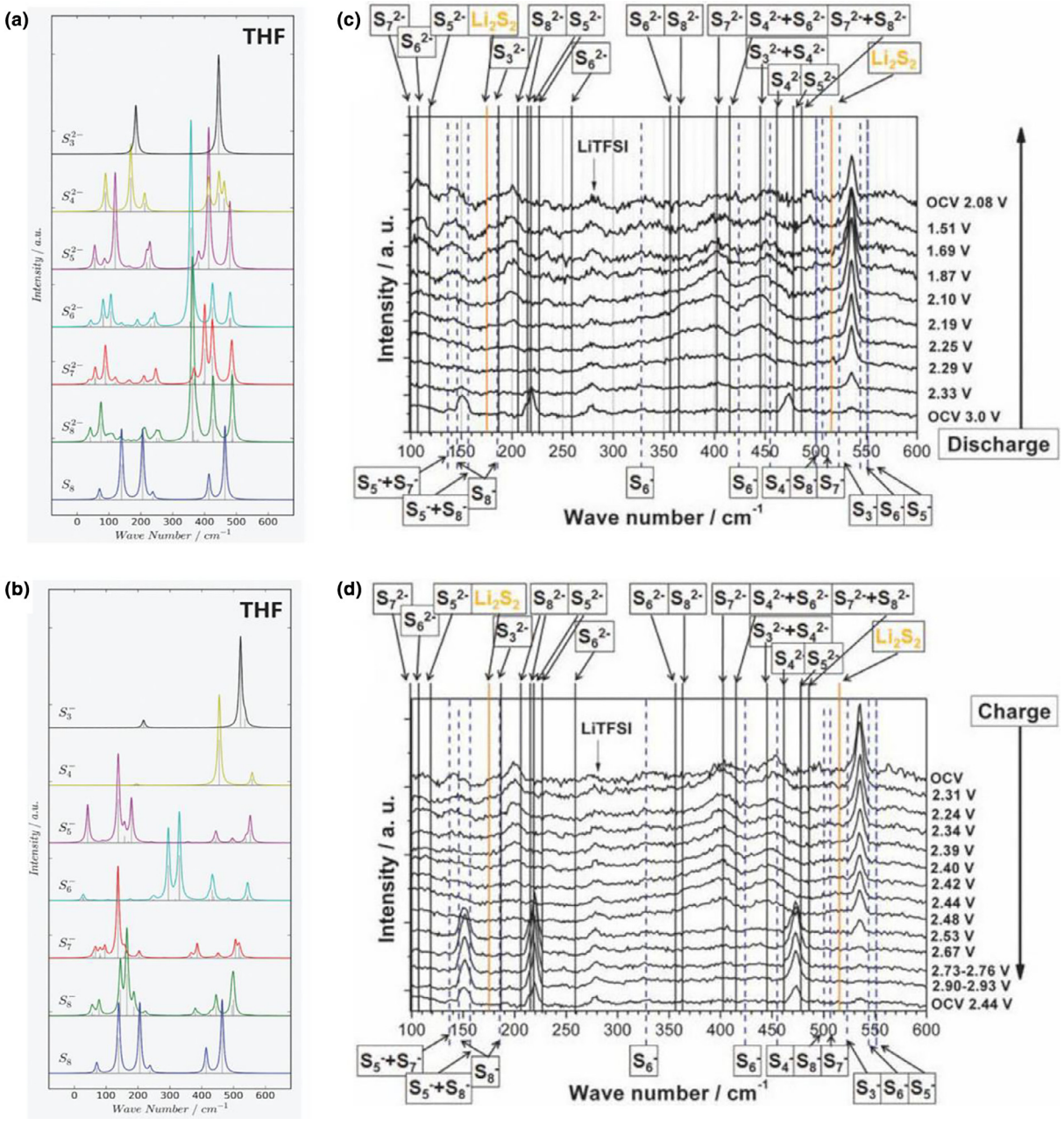

FIGURE 4

Examples of theoretical and experimental Raman spectroscopy, combined. Theoretical Raman spectra of individual (a) polysulfide di-anions S_n^{2-} and (b) polysulfide radical mono-anions S_n^{-} in THF solvent. In situ Raman spectra at various voltages during the (c) discharge and (d) charge processes. (Reprinted with permission from [144]. 2013, ECS.)

chemistry calculations can deconvolute the experimental spectra by providing a reliable artificial standard to fingerprint the characteristic peaks in experimental data. The theory can also provide insights into the origin of a specific experimental signal at the atomic and even electronic level. However, we emphasize the necessity of careful benchmarking between theory and experimental data, to ensure that an appropriate model for the system in question is obtained.

3.4. Binding energy

The shuttle effect is one of the major degradation mechanisms in Li–S systems, which refers to the spontaneous dissolution and diffusion of soluble polysulfide intermediates, causing a series of side reactions at the Li anode interface. The polysulfide shuttle-induced self-discharge induces the loss of active materials from the cathode, as well as renders a poor Coulombic efficiency and short cycling life. Significant efforts have been devoted to controlling the shuttle of polysulfides utilizing both physical and chemical confinement strategies. Graphene [54,71,72,74,75,179], CNTs [149,180–183], carbon nitrides [84], carbon nanofibers [184], polymers matrices [185–188], various metal oxides [97,98,189–195], sulfides [98,196–199], nitrides [200–203], carbides [204,205], other materials [206,207], and their hybrids [86,91,208,209] have been employed as sulfur

Please cite this article in press as: X. Chen et al., Materials Today, (2018), https://doi.org/10.1016/j.mattod.2018.04.007

TABLE 2

Calculated and experimental Raman vibrational frequencies of sulfur species. HMPA: Hexamethylphosphoramide; DMF: Dimethylformamide. Local symmetry of the vibrations: υ_s: Symmetric stretch vibration, υ_a: Antisymmetric stretch vibration, δ: Bending mode; Intensity: w = weak, m = medium, s = strong, vs = very strong. (Reprinted with permission from [144]· 2013, ECS.)

S_x^{y-}	Calculations[a] [144]	Experiments
S_2^-	560m (vacuum)	589 (NaI) [153,154], 594 (KI) [155]
S_3^-	**535** υ_s(SS), **522 m** υ_a(SS), 217w δ(SSS)	543 (KI) [155], 549 (NaI) [153], 535s, 232 in HMPA [156], 540 [157]; 534 (solid) [158], 535 (S_3^- in Li_2S_4 or Na_2S_4 in NH_3) [145], 535 (DMF) [153]
S_4^-	558m υ_s(SS, terminal), 500w, **455vs** υ_s(SS, central), 196w, 107w, 61w	518w, 439m, 384s (DMF) [153,154,159]
S_5^-	**552s**, 539m, 497m, 473vw, 445, 440m, 357w, 353w, 242w, 217w, **179s**, 170m, **158s**, **138s**, 89w, 50w, 44w, **42s**	
S_6^-	**544s**, 484w, **434s**, 423w, **329vs**, **295s**, 251w, 221w, 175w, 130w, 62w, 61w, 27m	
S_7^-	609m, 517m, 506m, 492m, 452w, 434w, 386m, 368w, 232w, 204w, 201w, 158w, 155w, **137s**, 96m, 80m, 66m	
S_8^-	500m, 495w, 445m, 437w, 429w, 391w, 380w, 224w, 216w, 196w, 187m, **165s**, 157, 145m, 78m, 62w, 56w, 55w	
S^{2-}	–	**372.6w** (Li_2S (+ paraffine)) [160], **378** [161]
S_2^{2-}	392 (vacuum), 428	473 (BaS_2) [154], 451 (ß-Na_2S_2) [154,162], **174** δ_s, **514** υ_s(SS) [163], 476, 469, 462, 454, 148, 118, 87 (K_2S_2 in NH_3) [164]
S_3^{2-}	**444s** υ_a(SS) and υ_s(SS) **184s** δ(SSS)	466s, 238m (K_2S_3) or 476–479s, 458m, 238w (Na_2S_3, BaS_3) [154,162,164], 479, 460, 256 (Na_2S_3 in NH_3) [164]
S_4^{2-}	**462s** υ_s(S–SS–S, terminal), **445s** υ_a(S–SS–S, terminal), **413s** υ_s(SS–SS, central), 212m, **168s**, **89s**	482s, 445m [154]; (Na_2S_4): aqueous: 484, 446, 410, 256, 194, 144; polycrystalline: 962, 935, 923, 883, 876, 482, 468, 445, 440, 239, 206, 171, 151, 97, 83, 48 [162]; (Li_2S_4 in NH_3, 293 K): 430vs, 188vs, (Na_2S_4 in NH_3, 293 K): 437vs, 191vs [145]
S_5^{2-}	**479s**, 473w, 413s, 381w, 228m, 219m, **119s**, 86w, 54m	496m, 432s, 252m (K_2S_5) [165], (Na_2S_5) [162]
S_6^{2-}	482m υ_s(S–SSSS–S, terminal), 479w υ_a(S–SSSS–S, terminal), 426m υ_s(SS–SS–SS), 425m υ_a(SS–SS–SS), **358 s** υ_s(SSS–SSS, central) 243w, 230w, 189w, 106m, 82m, 56w, 43w	453m, 373s, 358m, 337m, 254m (K_2S_6) [165]
S_7^{2-}	**486s** υ_s(S–SSSSS–S, terminal), 484w υ_a(S–SSSSS–S, terminal), 429w, **424s** **401s**, 368m υ_s(SSSS–SSS), 247m, 246m, 210w, 165w, 92s, 88w, 55m, 43w, 37w	
S_8^{2-}	**487s**, 486m, 443w, **427s**, 426m, 381w, **362s**, 258m, 250m 214m, 208m, 142w, 96w, 75s, 64w, 41m, 33w, 31w	

[a] If without any note, the calculation values are in THF solvent.

and polysulfide anchoring materials in the cathode host architecture. Hence, the molecular interaction strength between the soluble polysulfides and the host material is a widely used descriptor for rationally designed sulfur cathodes. As an example, the binding energy between Li_2S_4 and routine sulfur hosts is particularly summarized in Table 3.

Both experimental and theoretical methods have been applied to characterize the interaction strength between polysulfides and cathode materials. Experimentally, a signature of the interaction strength between host and soluble polysulfide is a rapid reduction in color of the polysulfide-containing solution. As an example, Cui and co-worker [101] investigated the interaction between polysulfides and a series of metal sulfides (Fig. 7). A 0.005 M Li_2S_6 solution was prepared by mixing sulfur with Li_2S in DOL/DME (1:1 by volume) solution. The obtained solution presents dark yellow color caused by soluble sulfur species (the Control in Fig. 7A). Nonpolar carbon materials (e.g., graphene, CNTs, and carbon black) exhibit almost no adsorption of lithium polysulfides and hence the combined solution presents the same color as that of the pristine solution. A lighter colored solution indicates a stronger adsorption ability of the corresponding metal sulfides. Both FeS and SnS_2 present a lighter color than that of G/CNT, indicating a stronger adsorption ability toward Li_2S_6. The original solutions become almost colorless after the addition of CoS_2, TS_2, and especially VS_2, which illustrates a high interaction between these three materials and the soluble polysulfides. Theoretically, the binding energy, which is defined as $E_b = E_M + E_{PS} - E_{M\text{-}PS}$ ($E_{M\text{-}PS}$, E_M, and E_{PS} are the total energy of metal sulfides bound with a lithium polysulfide, pristine metal sulfide, and lithium polysulfide, respectively), provides a descriptor that reflects the interaction strength between two species. A large positive binding energy indicates a strong adsorption of the sulfur host toward lithium polysulfides. Herein, the order of the binding energy of the metal sulfides is as follows: $VS_2 > TiS_2 > CoS_2 \gg FeS_2 > SnS_2 > Ni_3S_2$, which agrees well with the experimental trend shown in Fig. 7A. Similar methods have been applied to other sulfur hosts and the theoretical results show good agreement with the corresponding experimental trends [83,189,198,200].

An analogous periodic law has been proposed to explain the different binding energies of various first-row transition-metal sulfides [100]. The binding energy is strongly associated with the valence electron number of metal cations in metal sulfides. Specifically, V^{2+} has three single-valence electrons and electrons from sulfur can appropriately pair the three single electrons, inducing a strong anchoring effect. Simultaneously, Sc^{2+} and Ti^{2+} have insufficient valence electrons, and thus can only afford a weak interaction toward polysulfides. While Cu^{2+} has nine

Please cite this article in press as: X. Chen et al., Materials Today, (2018), https://doi.org/10.1016/j.mattod.2018.04.007

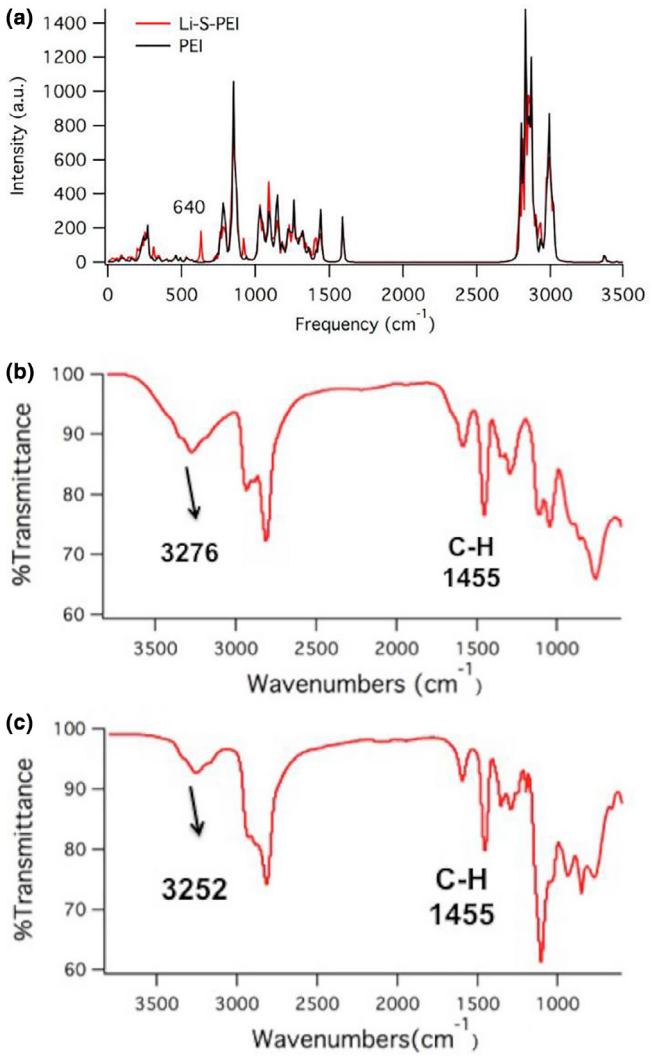

FIGURE 5

Examples of theoretical and experimental IR spectroscopy, combined. (a) Theoretical IR spectra of the mixture of Li–S species and PEI (red) and pure PEI (black). Experimental FTIR spectra of (b) pure PEI and (c) a mixture of lithium polysulfide and PEI. (Reprinted with permission from [149]. 2016, American Chemical Society.)

valence electrons, only one d-orbital with a vacancy can interact with the valence electrons of sulfur, which is responsible for the small binding energy.

The variational total energy of a molecule or system is the foundation upon which the DFT formulation rests. However, for practical system evaluations, some important considerations should be noted as follows:

(1) The selection of the absorbing crystal surface and its chemical state (e.g., surface termination and/or passivation layer) under the operating conditions are very important as different surface orientations and chemical terminations have different binding energies toward lithium polysulfides. When the transmission electron microscopy (TEM) or experimental XRD data are available, the experimentally measured exposed crystal surface should be chosen for modeling. Otherwise, it is recommended to compare the surface energy of different crystal surfaces and select the most stable surface with the lowest surface energy, under the operating conditions of the battery.

(2) The total energy is firstly determined by the intrinsic properties of materials, and further influenced by specific three-dimensional geometrical structures, such as various defects and core–shell structures, which can regulate the local electronic structure, and thus adjust the affinity of materials toward LiPSs.

(3) van der Waals forces should be included in the simulations, as the nonpolar bonding between polysulfides and sulfur hosts can exhibit a significant contribution from fluctuating and correlated polarization.

(4) The form of the adsorbed lithium polysulfide species needs to be deliberately considered. Recent AIMD [210] and MD [211] studies of the solvation structure in Li–S electrolyte indicate large cluster formation in lower order polysulfides, whereas reduced aggregation is observed with an increase in polysulfide chain length. However, in most studies, the simple contact ion pair structure (Li^+–S_n^-) is adopted during calculations for simplicity, which is quite straightforward for demonstrations.

(5) The fraction of coverage of polysulfides on the host materials should be considered in further studies. Currently, mostly the ideal low-density adsorption is considered. Notably, the binding strength changes with the rate of coverage of the adsorbent, similar to the adsorption of gas molecules in porous materials.

(6) A strong anchoring effect of hosts are highlighted in the most recent work [54,97,98,100,101]. However, we emphasize that, while an optimized binding strength is unknown, too strong interaction may result in decomposition of polysulfides, as well as inhibit the charging process.

3.5. NMR

A large body of theoretical works concerning the interaction between polysulfides and sulfur hosts have been performed, mostly focusing on binding energy, bond length, and charge analysis. A few studies highlight the electronic structure of the bonding to elucidate the chemical nature of the interaction. Taking the heteroatom-doped carbon materials as an example, polysulfides bind with the hosts through the Li···X interaction (X = N, O et al.), which can be denoted as a Li bond (Fig. 8A and B), analogous to the hydrogen bond. The partial covalent bond nature of H bond was considered controversial until ^{1}H NMR spectroscopy was employed to characterize the H bonded nuclei [212]. Similarly, ^{7}Li NMR spectroscopy may be a powerful tool for characterizing Li bonds. Zhang and co-workers [53] employed theoretical and experimental ^{7}Li NMR spectroscopy to explore the Li bond chemistry and its role in Li–S batteries. The peaks in ^{7}Li NMR spectra of Li_2S_8 exhibit an upshift of around 0.3 ppm with the presence of pyridine (PD) both in theoretical and experimental results (Fig. 8C and D). The upshift to the low field is ascribed to a de-shielding effect on the ^{7}Li atom, which is similar to that in H bond theory. Combined with binding energy, charge, and dipole analyses, the Li bond is categorized as a dipole–dipole like interaction and the upshift trend of ^{7}Li NMR peak is proposed as a quantitative descriptor of the Li bond strength. The Li bonds

Please cite this article in press as: X. Chen et al., Materials Today, (2018), https://doi.org/10.1016/j.mattod.2018.04.007

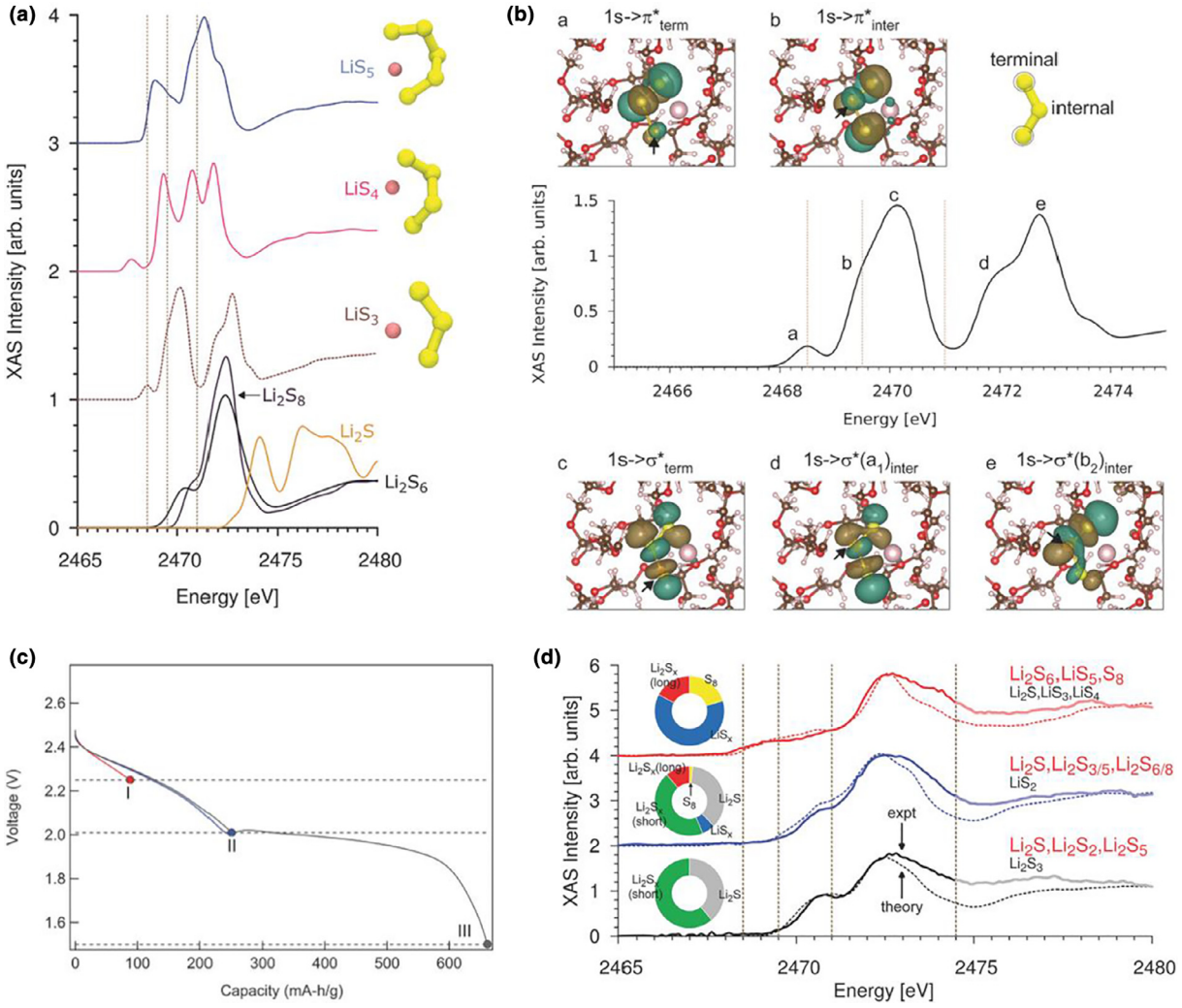

FIGURE 6

Combination of theory and experiment in XAS. (a) Calculated S K-edge XAS spectra of the solvated LiS_5 (blue), LiS_4 (pink), LiS_3 (brown), Li_2S_6 (black), Li_2S_8 (purple), and crystalline Li_2S (gold). (b) First-principles XAS spectra of the trisulfur LiS_3 molecule dissolved in tetraethylene glycol dimethyl ether (TEGDME). Each of the five major transitions that inform the spectra is indicated. Insets: representative electron density of the resulting excited states that the positive phase of the density is colored gold, while the negative phase is colored green. (c) The cell potential versus discharge capacity. (d) Comparison of the best-fit spectra from theory (dashed lines) and XAS measurements (solid lines) for each of the three voltages in (c). The hydrogen, lithium, carbon, oxygen, and sulfur atoms are marked with silver, pink, gray, red, and yellow, respectively. (Reprinted with permission from [166]. 2015, Wiley.)

in Li–S batteries facilitate the intermolecular binding, and thus enhance the kinetics of polysulfide conversion.

Besides sulfur cathodes, Li bond chemistry is supposed to afford new insights into electrolyte and Li metal anode studies. For example, while Li ions form very complicated complexes in electrolytes, Li bond chemistry is expected to help decipher these structures. Also, during the initial Li nucleation process, Li bonds are involved when solvated Li ions interact with anode conductive frameworks.

The above validation of Li bond chemistry presents a typical example of a constructive combination of theory and experiment. Indeed, the interaction between lithium polysulfides and host material exhibits varying degrees of complexity, depending on the host material and the architecture, as well as the components of the liquid electrolyte. Firstly, for example, for carbonaceous host materials, there are many forms. Even counting single atom-doped graphene spans the chemical space of pyridinic, pyrrolic, and graphitic nitrogen for nitrogen, ketone group, carboxylic group, epoxy group, cyclic group, hydroxyl group for oxygen, *etc*. Secondly, various electrolyte components, such as the Li salt, additives, and the solvents, can interact with the soluble polysulfides. In the abovementioned case, the authors adopted pyridine as the model molecule to investigate the interaction between polysulfides and the carbon host, and, fortuitously, the experimental ^{7}Li NMR results agreed well with the theoretical results.

In addition to the interaction between the Li atom and the host material, there is specific bonding characteristics between the sulfur atom in polysulfides and the metal in metal sulfide additives, denoted the sulfur bond [100]. Sulfur binding is considered even more complicated than lithium binding, and its mechanism is still not completely elucidated. Similarly, to the Li bond, NMR technology is expected to aid in clarifying the chemical nature of the sulfur binding chemistry.

Please cite this article in press as: X. Chen et al., Materials Today, (2018), https://doi.org/10.1016/j.mattod.2018.04.007

TABLE 3

The binding energy between Li_2S_4 and routine sulfur hosts.

Materials		Binding energy (eV)	Program and method[a]	Refs.
Carbon	Graphite	0.65	VASP/GGA/PBE/400 eV	[197]
	Graphene	0.70	$DMol^3$/GGA/PBE/–	[194]
	CNT	0.30	VASP/GGA/PBE/400 eV	[181]
Metal oxides	TiO_2	4.1	VASP/GGA/PBE/400 eV	[193]
	T_4O_7	4.2	VASP/GGA/PBE/400 eV	[193]
	V_2O_5	3.73	VASP/GGA/PBE/400 eV	[98]
	MoO_3	2.85	VASP/GGA/PBE/400 eV	[98]
	CeO_2	2.90	$DMol^3$/GGA/PBE/–	[194]
Metal sulfides	Co_9S_8	1.71	VASP/GGA/PBE/400 eV	[197]
	CoS_2	1.97	CASTEP/GGA/PBE/300 eV	[198]
	NbS_2	1.80	VASP/GGA/PBE/400 eV	[98]
	TiS_2	1.54	VASP/GGA/PBE/400 eV	[98]
	MoS_2	0.77	VASP/GGA/PBE/400 eV	[98]
	Ni_3S_2	2.2	VASP/GGA/PBE/400 eV	[199]
Metal nitrides	VN	3.27	$DMol^3$/GGA/PBE/–	[201]
	TiN	2.48	CASTEP/GGA/PBE/–	[203]
Metal carbides	TiC	1.89	$DMol^3$/GGA/PBE/4.5 Å	[190]
Others	$TiCl_2$	0.38	VASP/GGA/PBE/400 eV	[98]
	Phosphorene	1.27	$DMol^3$/GGA/PW91/5.1 Å	[206]
	C_3B	1.09	VASP/GGA/PBE/520 eV	[207]

[a] The first: program; the second and third: exchange–correlation functional; the fourth: cutoff energy.

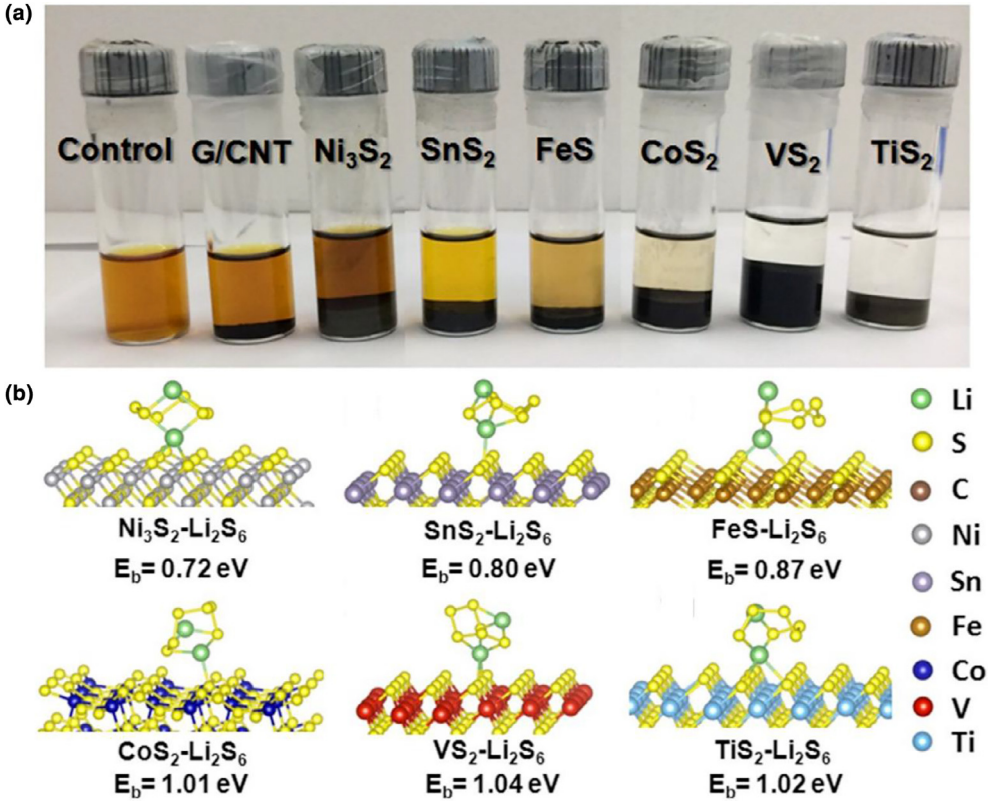

FIGURE 7

Combination of theory and experiment in the adsorption strength of sulfur hosts toward lithium polysulfides. (a) Digital image of the Li_2S_6 (0.005 M) captured by carbon and metal sulfides in DOL/DME solution. (b) Atomic conformations and binding energy for Li_2S_6 species adsorption on various metal sulfides. Here, green, yellow, gray, purple, brown, blue, red, and cyan balls represent lithium, sulfur, nickel, tin, iron, cobalt, vanadium, and titanium atoms, respectively. (Reprinted with permission from [101]. 2017, NAS.)

Please cite this article in press as: X. Chen et al., Materials Today, (2018), https://doi.org/10.1016/j.mattod.2018.04.007

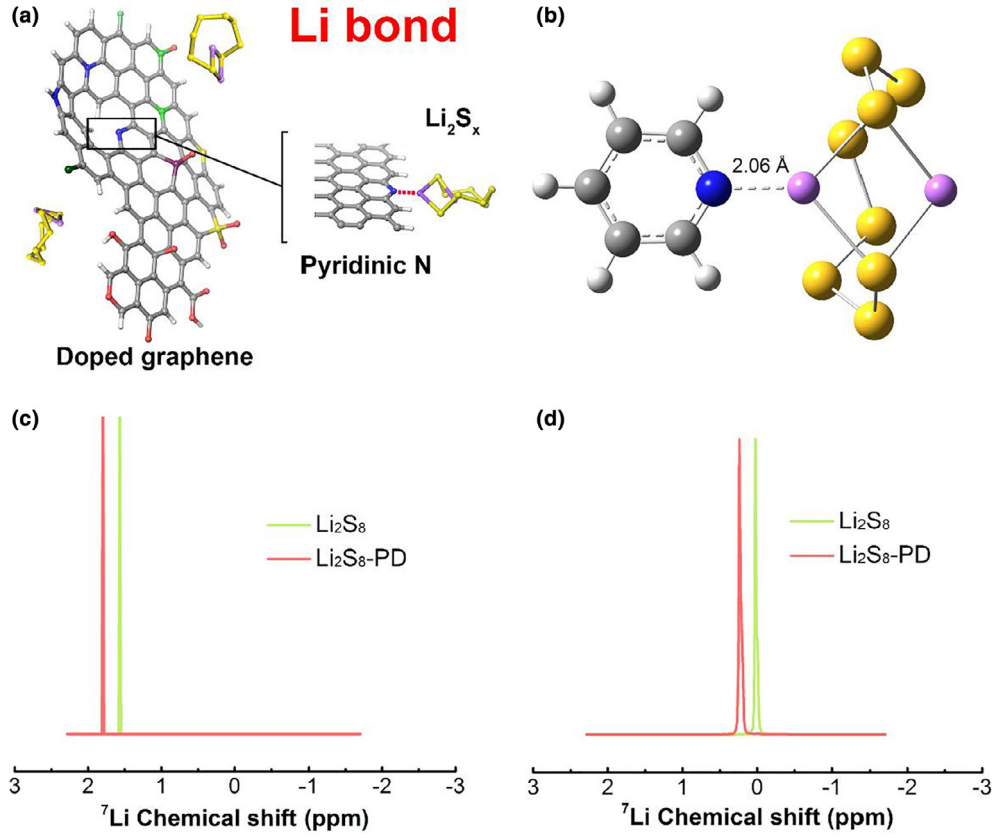

FIGURE 8

Combination of theory and experiment in NMR. (a) The schematic diagrams of the lithium bond in a Li–S cell. (b) Modeling of lithium bonds. (c) Theoretically calculated and (d) experimentally obtained ^{7}Li NMR spectra of Li_2S_8 before and after interacting with PD molecule. PD: pyridine. Gray, blue, white, purple and yellow spheres are C, N, H, Li, and S atoms, respectively. (Reprinted with permission from [53]. 2017, Wiley.)

3.6. Others

Computational chemistry can also play a very important role in other aspects of Li–S battery researches, such as investigating the stability and decomposition mechanism of electrolytes, constructing lithiophilic frameworks for Li metal anodes, and rationally designing a stable SEI. In these aspects, theoretical simulations mainly afford a deep insight into the experimental phenomena or provide a theoretical guidance for further experiments. Besides, other characterization techniques that can possibly combine with theoretical analyses are also provided in this part.

Due to the high reactivity of lithium metal, routine organic electrolytes decompose seriously on the anode. Although the reaction pathway of electrolyte decomposition has been well examined [213–215], the chemical origin of the instability of organic electrolytes on Li metal anodes is not clear. Recently, Chen et al. proposed that ion–solvent complexes promote the electrolyte decomposition on lithium metal anode [102]. The LUMO (the lowest unoccupied molecular orbital) level of electrolyte solvents is obviously reduced once coordinated with lithium ions, indicating the enhanced reduction activity of electrolytes, which is responsible for the continuous electrolyte degradation in working cells. The in situ optical microscopic observations further validated the theoretical predictions that the gassing of electrolyte with Li salts is much more violent than pure solvents. Inspired from the theoretical and experimental results, the authors further proposed two perspectives on electrolyte design. Firstly, compared with conventionally used redox potential of organic solvent, the redox potential of ion–solvent complexes is more suitable as parameters for electrolyte screening. Secondly, introducing a different cation into the system is expected to influence the solvation structure, and thus either stabilize the electrolyte or optimize the SEI. Therefore, this principle uncovers the critical role of ion–solvent complexation for the stability of lithium metal anodes and delivers a rational design strategy for stable electrolyte.

Since most organic solvents are intrinsically reducible by Li while ion–solvent complexes are ubiquitous in any known electrolyte system, designing an artificial or in situ protective layer on the metal anode to prevent its direct exposure to unstable ion–solvent complexes emerges as a more promising and feasible approach to suppress electrolyte decomposition than searching for a "stable" solvent [57,102]. Currently, various electrolyte additives have been applied to induce a stable in situ SEI on Li metal anodes. For example, fluoroethylene carbonate (FEC) with a lower LUMO level than that of routine electrolyte solvents, such as ethylene carbonate (EC) and diethyl carbonate (DEC), is preferential to be reduced on Li metal anodes [116]. The decomposed FEC is beneficial for the formation of a robust LiF-rich SEI, on which EC and DEC are stable. In addition, the LiF-

Please cite this article in press as: X. Chen et al., Materials Today, (2018), https://doi.org/10.1016/j.mattod.2018.04.007

rich SEI can also induce a stable lithium plating/stripping with columnar morphology and a dendrite-free feature [110]. Other electrolyte additives or Li salt, such as lithium bis(fluorosulfonyl)imide (LiFSI) [216], lithium iodide (LiI) [217], and lithium bromide (LiBr) [218], have been comprehensively investigated by Yushin and co-workers. In the LiFSI-based electrolytes, LiF and FSI(−F) anion radical form during LiFSI–DME reduction at 1.5–1.6 V vs. Li/Li^+. The FSI(−F) anion radical can further induce a H-transfer reaction from DME to SO_2-group of FSI(−F) and the as-generated DME(−H) radical can readily participate the polymerization reaction, thus inducing a stable SEI. The LiI and LiBr additives promote the polymerization of DME through similar mechanism. The Li salt and additives not only induce an in situ protective coating on the anode but also on the cathode surface.

Artificial protective layers, which are stable against lithium metal anode, are also considered to stabilize the electrolyte–anode interface. Mo and co-workers presented a systematic investigation of lithium-stable materials across the periodic table through first-principles calculations [219]. While most oxides, sulfides, and halides are predicted to be reduced by lithium metal due to the reduction of metal cations, nitride anion exhibits unique stability against Li metal, which is either intrinsically stable or due to passivation. Tian et al. investigated various 2D layered materials, including h-BN, graphene, silicene, germanene, stanene, phosphorene, SnS, and SnSe, as the protective films for Li metal anodes [108]. To ensure efficient Li ions migration through these 2D-layered materials, the introduction of defects into 2D materials is necessary, which, however, simultaneously reduces the stiffness of the layer against the suppression of dendrite growth. Therefore, a balance between the Li ion migration and stiffness is required. These two works afford a general strategy for the rational design of artificial SEI on Li metal anodes.

Designing Li metal hosts with uniform lithiophilic sites that can guide an even Li deposition is another approach to build a stable Li metal anode. For instance, various carbon materials, including graphene [220], CNTs [221], and carbon fibers [222], have employed as the anode frameworks. Particularly, nitrogen-doped graphene (NG) has been adopted as the Li-plating matrix to guide Li metal nucleation, delivering dendrite-free morphology, low nucleation overpotential, and improved Coulombic efficiency [220]. The excellent lithiophilicity of NG was demonstrated by the first-principles calculations in combination with Li nucleation overpotential test. Besides, the lithiophilicity of rGO [223] and Ag nanoparticles [224] was also validated by theoretical simulations. Computational chemistry have afforded fruitful insights into the lithiophilicity chemistry and delivered a rational strategy for designing lithiophilic frameworks to induce a stable Li metal anode.

Theoretical simulations can also combine with other experimental techniques. For example, X-ray photoelectron spectroscopy (XPS) is widely used to investigate the chemical state and component of materials, and the peak of binding energy in XPS is strongly associated with atomic valence states. Due to challenges associated with the treatment of core electrons and the steep and poorly screened Coulomb potential near the nucleus, it is hard to calculate the absolute binding energy in XPS spectrum [225]. However, it has been validated that binding energy shifts can be obtained by DFT calculation [226]. Besides, DFT can determine the crystal structure [227] with the aid of searching algorism, providing a reference to experimental structure identification, such as scanning tunneling microscopy (STM) and scanning transmission electron microscopy (STEM). Actually, DFT calculations and STM/STEM have already been applied together to other researches beyond Li–S batteries [228]. This integration is strongly expected to be applied in Li–S studies in the near future.

4. The "Collaboration" in the future

Three emerging endeavors including high-accuracy calculations with large-scale models, materials genome, and machine-learning approaches are anticipated to promote the combination of theory and experiments in the near future. High-accuracy calculations, as well as large-scale models, will improve the relevance of current model systems, and bring them closer to realistic environments. Moreover, the recently proposed concept of material genome affords the possibility of high-throughput screening of materials by proper descriptors, predicting optimal chemical and structure formulations, thus guiding future experiments. As larger data sets are obtained, both from calculations and experiments, machine-learning models may be employed to extract trends, accelerating the time to prediction. In the following, a brief introduction of these methods and their potential applications in Li–S batteries are provided.

4.1. High-accuracy calculations and large-scale models

Quantum chemistry methods specialize in micro-scale studies, especially at the level of atoms or small molecules, while becoming prohibitively slow for larger systems. Hence, phenomena that rely on cooperative behavior involving hundreds–thousands of atoms, as well as systems with intrinsic defects or impurities, may not be well described and present current gaps between theoretical and experimental approaches.

Firstly, effectively leveraging high-performance computing, algorithmic development, and software improvement may narrow the disparity between theory and experiment. For example, instead of using simple single-molecule models, the adsorption, as well as the nucleation, process of lithium polysulfide on conductive frameworks can be studied with more accurate cluster models. Recently, Zhao and co-authors [229] performed DFT calculation to investigate the delithiation of lithium polysulfides on silicene and borophene surfaces with LiPSs or sulfur clusters fully covering the surfaces. Liu et al. [230] described the formation of the Li_2S film on lithium anode surface using AIMD simulation, and a different coverage was considered.

Concurrently, the development of efficient software infrastructure may also enable the handling of larger and more complicated chemical systems [44]. For example, Persson et al. [211] used MD simulations with well-benchmarked, effective non-polarizable potentials to investigate the solvation behavior of Li–S electrolyte with a large model with thousands of molecules (Fig. 9A and B). The formation of large clusters of lower order polysulfides and the increasing chain lengths of longer polysulfides were demonstrated, highlighting the important role of solvation effects.

Please cite this article in press as: X. Chen et al., Materials Today, (2018), https://doi.org/10.1016/j.mattod.2018.04.007

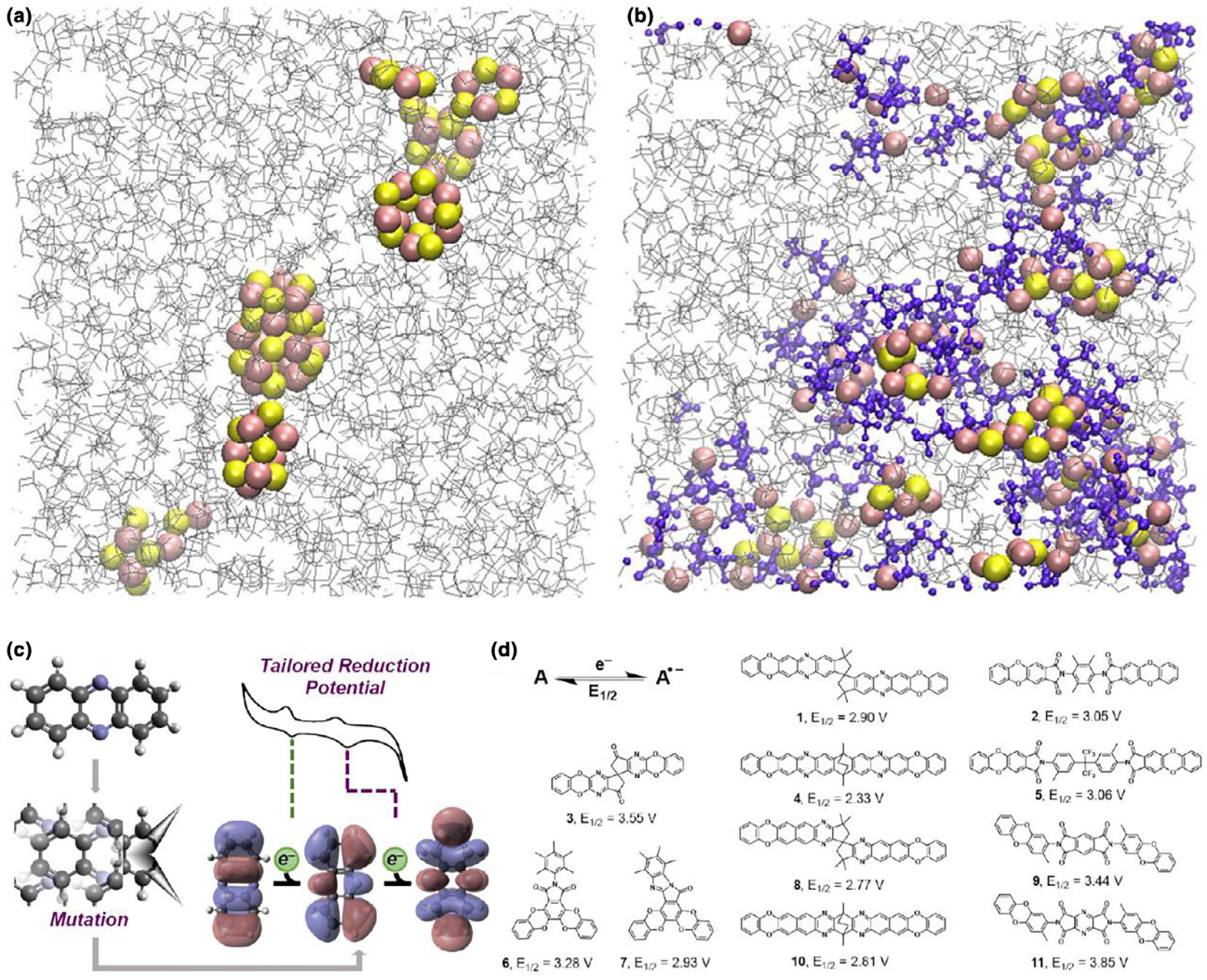

FIGURE 9

Representative simulation snapshot of (a) Li_2S_2/DOL:DME, (b) (Li_2S_2 + LiTFSI)/DOL:DME at 298 K. Li^+: pink ball; S_2^{2-}: yellow ball; $TFSI^-$: blue licorice; DME and DOL: gray line. LiTFSI: bis(trifluoromethane)sulfonimide lithium salt. Predictive design of polymer membranes for Li–S batteries. (Reprinted with permission from [211]. 2017, American Chemical Society.) (c) The library of redox-active monomer segments, generated and screened through materials genome. (d) PIM–monomer segments with reduction potentials ($E_{1/2}$) higher than 2.5 V *vs.* Li/Li^+. (Reprinted with permission from [240]. 2017, American Chemical Society.)

Finally, the improved accuracy of computational methods and new algorithms to simulate and understand chemical systems are necessary. For example, beyond the "generalized gradient approximation" (GGA), "meta-GGA", and hybrid functionals (such as B3LYP [231–233]) are adopted to further improve the accuracy of DFT calculations. The emerging machine-learning technique can even bypass the Kohn–Sham equations through learning the energy functional via examples [234]. The complex and competitive bonding in Li–S batteries, including the complicated interfacial interactions between electrolytes and electrodes, are expected to require advanced methodologies for complete description of correlated electron effects, polarization, and charge transfer. The emerging energy decomposition analysis (EDA) [235–238] of electronic structure calculations can help facilitate quantitative understanding of diverse intermolecular interactions and also develop molecular mechanical force field parameters. Electronic, as well as ionic, transport in crystalline or amorphous discharge products will be further explored with more powerful computers, high-accuracy calculation methods, and large-scale models.

4.2. Materials genome

The idea of a materials genome is to predict, screen, and optimize materials at an unparalleled scale and rate through the tight integration of computational, experimental, and data science methodologies. With the advent of high-throughput computational approaches and associated databases, such as the Materials Project [239], today's materials scientists can access tens of thousands of materials at the same time and screen them by required properties, such as the geometry, electronic structure, discharge curve, total gravimetric/volumetric capacity, energy density, specific energy, volume change, and reactivity [240–244]. Helms and coauthors [240] implemented the material genome to screen a library of monomer segments for the design of an ion-selective separator for Li–S batteries (Fig. 9C and D). As a result, a high-performance membrane was rationally configured from a class

Please cite this article in press as: X. Chen et al., Materials Today, (2018), https://doi.org/10.1016/j.mattod.2018.04.007

of redox-switchable polymers of intrinsic microporosity (PIM) using the selected monomer, achieving both high selectivity and high ionic conductivity. Other successful examples include high-throughput screening procedures for LIBs, as well as solid-state electrolytes with super lithium ion conductivity and stability using bond-valence (BV) methods and DFT [245]. For example, Ceder and co-workers [246–248] screened a series of materials as the potential cathode materials for LIBs, such as Li_x-$M(YO_3)(XO_4)$ (Y = S, P, Si, As; X = C, B; M = redox-active metal; and x = 1–3). However, a high-throughput screening for Li–S cathode materials and additives is lacking.

Many recent theoretical works concerning the electrode materials design of sulfur cathodes have focused on the shuttle effects, using the host–polysulfide binding energy as a descriptor for the sulfur cathode rational design. However, as noted in Section 3.4, the calculation of binding energy is strongly affected by many factors, such as the choice of computational method and the details of the chemical and structural materials modeling. A standard database, comprising bonding information, chemical and electrochemical stability, and lithium ion and electron conductivity, using a unified evaluation method with considerable accuracy, would significantly contribute toward improved understanding and descriptor development for the future development of Li–S batteries.

4.3. Machine learning

When large data sets are available, either by experimental or theoretical means, machine learning can help us understand the underlying trends by heuristic, predictive models or functions trained on the existing data. Machine-learning methods can be particularly useful in clarifying complex data landscapes, where the driving forces are comprised by a combination of physical interactions and chemical reactions. However, although machine-learning techniques have been successfully applied to various areas of materials science [48,249–255], to the best of our knowledge, they have not been applied to Li–S batteries, for example, in the prediction of optimal anchoring materials by tailoring a suitable binding energy toward lithium polysulfides. It is expected that the lack of large, organized, systematic, and robust data is the underlying reason for this discrepancy. Hence, we anticipate that high-throughput computations can provide the remedy in the development of such suitable data and associated databases.

On the basis of above discussions, much effort should be devoted to the following aspects to bridge the gap between theory and experiment in Li–S researches. Firstly, an open source platform and database for Li–S batteries is urgently required. A well-established database that contains the theoretical FTIR, XAR, and other spectroscopy, as well as fundamental physical/-chemical properties of electrode or electrolyte materials, can provide an excellent reference for experimental results, and thus promote the collaboration. Secondly, high-throughput screening of electrode or electrolyte materials can be achieved by the emerging machine-learning technique once a user-friendly database has been constructed. Thirdly, not only new materials but also new synthetic methodology should be explored, in which theoretical simulations can also play an important role in combination with artificial intelligence. For example, machine learning can guide material discovery based on current knowledge [48].

5. Summary and outlook

Owing to the significant developments of quantum chemistry and computer science, theory and experiment are poised to play equally important roles in the future development of chemistry and materials science. In this review, we have summarized the recent progress in computational approaches applied to Li–S batteries, divided into four parts, structure, spectroscopy, thermodynamics, and kinetics. Specifically, we highlight instances where theoretical methods provide synergistic information alongside experimental characterizations, such as XRD, IR & Raman spectra, XAS, binding energy, and NMR analyses. We also call out areas where challenges remain such as the integration of theory and experiment due to intrinsic gaps between model and realistic systems, approximations in theoretical descriptions and the interpretation of experimental results. The recent development of theoretical and computational chemistry, including high-accuracy methodologies, numerical treatment of larger systems, materials genome methods, and machine learning, are likely to contribute positively toward bridging the gaps in the near future and promote the understanding and advancement of the Li–S battery, as well as other fields of studies.

Acknowledgments

This work was supported by National Key Research and Development Program (2016YFA0202500, 2016YFA0200102, and 2015CB932500), and National Natural Scientific Foundation of China (21676160). Tingzheng Hou and Kristin A. Persson were supported by the Battery Materials Research (BMR) program, under the Assistant Secretary for Energy Efficiency and Renewable Energy, Office of Vehicle Technologies of the U.S. Department of Energy, Contract No. DE-AC02-05CH11231. We thank Prof. Bo Li, Prof. Jun Li, Prof. Jia-Qi Huang, and Hong-Jie Peng for helpful discussion.

References

[1] D. Larcher, J.M. Tarascon, Nat. Chem. 7 (2015) 19–29.
[2] M. Armand, J.M. Tarascon, Nature 451 (2008) 652–657.
[3] M.R. Palacin, A. de Guibert, Science 351 (2016) 1253292.
[4] X.B. Cheng et al., Chem. Rev. 117 (2017) 10403–10473.
[5] T. Nagaura, K. Tozawa, Prog. Batteries Solar Cells 9 (1990) 209.
[6] J. Janek, W.G. Zeier, Nat. Energy 1 (2016) 16141.
[7] X. Zhang et al., J. Energy Chem. 25 (2016) 967–984.
[8] P.G. Bruce et al., Nat. Mater. 11 (2012) 19–29.
[9] H.-J. Peng et al., Adv. Energy Mater. 7 (2017) 1700260.
[10] Z.W. Seh et al., Chem. Soc. Rev. 45 (2016) 5605–5634.
[11] M. Wild et al., Energy Environ. Sci. 8 (2015) 3477–3494.
[12] L. Li et al., Science 359 (2018) 1513–1516.
[13] A. Manthiram et al., Acc. Chem. Res. 46 (2013) 1125–1134.
[14] A. Manthiram et al., Adv. Mater. 27 (2015) 1980–2006.
[15] R. Fang et al., Adv. Mater. 29 (2017) 1606823.
[16] A. Manthiram et al., Chem. Rev. 114 (2014) 11751–11787.
[17] H.J. Peng et al., Chem. Soc. Rev. 46 (2017) 5237–5288.
[18] T. Wang et al., Small Methods 1 (2017) 1700089.
[19] Y.X. Yin et al., Angew. Chem. Int. Ed. 52 (2013) 13186–13200.
[20] X. Ji et al., Nat. Mater. 8 (2009) 500–506.
[21] G. Zhang et al., Small Methods 1 (2017) 1700134.
[22] J. Lochala et al., ACS Appl. Mater. Interfaces 9 (2017) 24407–24421.
[23] P. Bonnick et al., J. Electrochem. Soc. 165 (2018) A6005–A6007.
[24] G. Li et al., Chem 4 (2018) 3–7.
[25] M.J. Klein et al., J. Am. Chem. Soc. 139 (2017) 10669–10676.

Please cite this article in press as: X. Chen et al., Materials Today, (2018), https://doi.org/10.1016/j.mattod.2018.04.007

[26] C.-H. Chang et al., Energy 6 (2017) 72–78.
[27] J.T. Lee et al., Adv. Mater. 25 (2013) 4573–4579.
[28] F. Wu et al., Adv. Mater. 27 (2015) 5579–5586.
[29] X. Liu et al., Adv. Mater. 29 (2017) 1601759.
[30] L. Borchardt et al., Chem. Eur. J. 22 (2016) 7324–7351.
[31] L. Ma et al., Nano Today 10 (2015) 315–338.
[32] M.A. Pope, I.A. Aksay, Adv. Energy Mater. 5 (2015) 1500124.
[33] Z. Li et al., Energy Environ. Sci. 9 (2016) 3061–3070.
[34] R. Zhang et al., Adv. Sci. 4 (2017) 1600445.
[35] D. Lin et al., Nat. Nanotechnol. 12 (2017) 194–206.
[36] R. Cao et al., Adv. Energy Mater. 5 (2015) 1402273.
[37] T. Tao et al., Adv. Mater. 29 (2017) 1700542.
[38] J.-Q. Huang et al., Energy Storage Mater. 1 (2015) 127–145.
[39] L. Cheng et al., ACS Energy Lett. 1 (2016) 503–509.
[40] Q. Pang et al., Nat. Energy 1 (2016) 16132.
[41] Y.-Z. Sun et al., Sci. China Chem. 60 (2017) 1508–1526.
[42] W. Chen et al., Adv. Energy Mater. 8 (2018) 1702348.
[43] S. Zhang et al., Adv. Energy Mater. 5 (2015) 1500117.
[44] S. Grimme, P.R. Schreiner, Angew. Chem. Int. Ed. (2017), https://doi.org/10.1002/anie.201709943.
[45] R.O. Jones, Rev. Mod. Phys. 87 (2015) 897–923.
[46] M.G. Medvedev et al., Science 355 (2017) 49–52.
[47] A. von Lilienfeld, Angew. Chem. Int. Ed. (2017), https://doi.org/10.1002/anie.201709686.
[48] P. Raccuglia et al., Nature 533 (2016) 73–76.
[49] E.O. Pyzer-Knapp et al., Adv. Funct. Mater. 25 (2015) 6495–6502.
[50] X. Qu et al., Comput. Mater. Sci. 103 (2015) 56–67.
[51] L. Cheng et al., J. Phys. Chem. Lett. 6 (2015) 283–291.
[52] R. Gómez-Bombarelli et al., Nat. Mater. 15 (2016) 1120.
[53] T.Z. Hou et al., Angew. Chem. Int. Ed. 56 (2017) 8178–8182.
[54] T.Z. Hou et al., Small 12 (2016) 3283–3291.
[55] L. Ma et al., Adv. Energy Mater. 4 (2014) 1400390.
[56] R.S. Assary et al., J. Phys. Chem. C 118 (2014) 11545–11558.
[57] X. Chen et al., Energy Storage Mater. 8 (2017) 194–201.
[58] R. Ferrando et al., Chem. Rev. 108 (2008) 845–910.
[59] D. Xiang et al., Chem. Rev. 116 (2016) 4318–4440.
[60] R. Roldan et al., Chem. Soc. Rev. 46 (2017) 4387–4399.
[61] R.A. Mata, M.A. Suhm, Angew. Chem. Int. Ed. 56 (2017) 11011–11018.
[62] J. Song et al., Adv. Funct. Mater. 24 (2014) 1243–1250.
[63] G. Li et al., Adv. Energy Mater. 7 (2017) 1702381.
[64] S. Ji et al., Chem. Eur. J. 23 (2017) 18208–18215.
[65] X.-B. Cheng et al., Nano Energy 4 (2014) 65–72.
[66] H.J. Peng et al., Adv. Mater. Interfaces 1 (2014) 1400227.
[67] D. Gueon et al., ACS Nano 12 (2018) 226–233.
[68] W. Yang et al., Nanoscale 10 (2018) 816–824.
[69] L. Fei et al., Adv. Mater. 27 (2015) 5936–5942.
[70] Z. Wang et al., Nat. Commun. 5 (2014) 5002.
[71] G. Zhou et al., Nat. Commun. 6 (2015) 7760.
[72] G. Zhou et al., ACS Nano 7 (2013) 5367–5375.
[73] C. Tang et al., Adv. Funct. Mater. 26 (2016) 577–585.
[74] H.J. Peng et al., ACS Nano 8 (2014) 11280–11289.
[75] G.M. Zhou et al., Adv. Energy Mater. 6 (2016) 1501355.
[76] Y. You et al., J. Mater. Chem. A 3 (2015) 4799–4802.
[77] G. Tan et al., Nat. Energy 2 (2017) 17090.
[78] F. Wu et al., ACS Nano 10 (2016) 1333–1340.
[79] L. Ji et al., J. Am. Chem. Soc. 133 (2011) 18522–18525.
[80] Z.W. Seh et al., Chem. Sci. 5 (2014) 1396.
[81] C. Yao et al., RSC Adv. 8 (2018) 3443–3452.
[82] X. Xu et al., RSC Adv. 8 (2018) 5298–5305.
[83] C.Y. Chen et al., Adv. Mater. 29 (2017) 1606802.
[84] J. Liang et al., ACS Appl. Mater. Interfaces 8 (2016) 25193–25201.
[85] M.Q. Zhao et al., ACS Nano 6 (2012) 10759–10769.
[86] H.J. Peng et al., Adv. Funct. Mater. 24 (2014) 2772–2781.
[87] Y.-L. Ding et al., Adv. Funct. Mater. 26 (2016) 1112–1119.
[88] J. Song et al., Angew. Chem. Int. Ed. 54 (2015) 4325–4329.
[89] G. Hu et al., Adv. Mater. 28 (2016) 1603–1609.
[90] N.-W. Li et al., RSC Adv. 6 (2016) 617–622.
[91] G.M. Zhou et al., Adv. Energy Mater. 5 (2015) 1402263.
[92] H. Pan et al., Adv. Funct. Mater. 27 (2017) 1703936.
[93] C. Hu et al., Nat. Commun. 8 (2017) 479.
[94] M.J. Klein et al., J. Am. Chem. Soc. 139 (2017) 9229–9237.
[95] L. Luo, A. Manthiram, ACS Energy Lett. 2 (2017) 2205–2211.
[96] S.-H. Chung, A. Manthiram, Adv. Mater. 30 (2018) 1705951.
[97] X. Tao et al., Nat. Commun. 7 (2016) 11203.
[98] Q. Zhang et al., Nano Lett. 15 (2015) 3780–3786.
[99] C.J. Hart et al., Chem. Commun. 51 (2015) 2308–2311.
[100] X. Chen et al., ACS Energy Lett. 2 (2017) 795–801.
[101] G. Zhou et al., Proc. Natl. Acad. Sci. U.S.A. 114 (2017) 840–845.
[102] X. Chen et al., Angew. Chem. Int. Ed. 57 (2018) 734–737.
[103] R. Zhang et al., Adv. Mater. 28 (2016) 2155–2162.
[104] X. Liang et al., Nat. Energy 6 (2017) 17119.
[105] T.T. Zuo et al., Adv. Mater. 29 (2017) 1700389.
[106] X.B. Cheng et al., Energy Storage Mater. 10 (2018) 199–205.
[107] Y. Liu et al., Adv. Mater. 29 (2017) 1605531.
[108] H.Z. Tian et al., Adv. Energy Mater. 7 (2017) 1602528.
[109] X.B. Cheng et al., Chem 2 (2017) 258–270.
[110] X.Q. Zhang et al., Angew. Chem. Int. Ed. 56 (2017) 14207–14211.
[111] J.T. Lee et al., ACS Energy Lett. 1 (2016) 373–379.
[112] R. Khurana et al., J. Am. Chem. Soc. 136 (2014) 7395–7402.
[113] Z. Tu et al., Small 11 (2015) 2631–2635.
[114] C.-Z. Zhao et al., Proc. Natl. Acad. Sci. U.S.A. 114 (2017) 11069–11074.
[115] X.B. Cheng et al., Nat. Commun. 8 (2017) 336.
[116] X.-Q. Zhang et al., Adv. Funct. Mater. 27 (2017) 1605989.
[117] M. Shimizu et al., PCCP 20 (2018) 1127–1133.
[118] A. Jozwiuk et al., Energy Environ. Sci. 9 (2016) 2603–2608.
[119] H. Schneider et al., Electrochim. Acta 243 (2017) 26–32.
[120] L. Zhang et al., J. Phys. Chem. C 121 (2017) 15549–15555.
[121] H.R. Jiang et al., J. Mater. Chem. A 6 (2018) 2107–2114.
[122] S. Li et al., PCCP 19 (2017) 32708–32714.
[123] G.S. Yi et al., PCCP 19 (2017) 28189–28194.
[124] Y. Zhao et al., PCCP 19 (2017) 18208–18216.
[125] Y. Zhao, J. Zhao, Appl. Surf. Sci. 412 (2017) 591–598.
[126] Y. Zheng et al., Appl. Surf. Sci. 434 (2018) 596–603.
[127] L.-C. Yin et al., Nano Energy 25 (2016) 203–210.
[128] Q. Liu et al., RSC Adv. 7 (2017) 33373–33377.
[129] K.C. Wasalathilake et al., RSC Adv. 8 (2018) 2271–2279.
[130] T. Zhu et al., ChemElectroChem 4 (2017) 2975–2980.
[131] J.C. Burgos et al., J. Phys. Chem. C 121 (2017) 18369–18377.
[132] E.S. Sim et al., J. Power Sources 342 (2017) 64–69.
[133] D. Rao et al., Carbon 110 (2016) 207–214.
[134] G. Zhou et al., ACS Cent. Sci. 4 (2018) 260–267.
[135] S. Li et al., ACS Energy Lett. 1 (2016) 481–489.
[136] D.-G. Oei, Inorg. Chem. 12 (1973) 438–441.
[137] J.A. Gladysz et al., Tetrahedron 35 (1979) 2329–2335.
[138] R.D. Shannon, Acta Crystallogr., Sect. A 32 (1976) 751–767.
[139] J. Kao, J. Mol. Struct. 56 (1979) 147–152.
[140] L.J. Wang et al., J. Energy Chem. 22 (2013) 72–77.
[141] A. Kawase et al., PCCP 16 (2014) 9344–9350.
[142] Z. Feng et al., J. Power Sources 272 (2014) 518–521.
[143] A. Paolella et al., J. Power Sources 325 (2016) 641–645.
[144] M. Hagen et al., J. Electrochem. Soc. 160 (2013) A1205–A1214.
[145] P. Dubois et al., Inorg. Chem. 27 (1988) 73–80.
[146] T. Chivers, P.J.W. Elder, Chem. Soc. Rev. 42 (2013) 5996–6005.
[147] K. Dokko et al., J. Electrochem. Soc. 160 (2013) A1304–A1310.
[148] R. Steudel, Top. Curr. Chem. 231 (2003) 127–152.
[149] L. Ma et al., ACS Nano 10 (2016) 1050–1059.
[150] M. Yu et al., Energy Environ. Sci. 9 (2016) 1495–1503.
[151] Q. Pang, L.F. Nazar, ACS Nano 10 (2016) 4111–4118.
[152] S. Evers et al., J. Phys. Chem. C 116 (2012) 19653–19658.
[153] R.J.H. Clark, D.G. Cobbold, Inorg. Chem. 17 (1978) 3169–3174.
[154] T. Chivers, C. Lau, Inorg. Chem. 21 (1982) 453–455.
[155] J.M. Hayes, S.M. Bachrach, J. Phys. Chem. A 107 (2003) 7952–7961.
[156] T. Chivers, I. Drummond, Inorg. Chem. 11 (1972) 2525–2527.
[157] P. Leghié et al., Electrochem. Commun. 4 (2002) 406–411.
[158] M.W. Wong, Top. Curr. Chem. 231 (2003) 1–29.
[159] F. Seel et al., Pure Appl. Chem. 49 (1977) 45–54.
[160] B. Bertheville et al., J. Phys.: Condens. Matter. 10 (1998) 2155–2169.
[161] J.T. Yeon et al., J. Electrochem. Soc. 159 (2012) A1308–A1314.
[162] G.J. Janz et al., Inorg. Chem. 15 (1976) 1759–1763.
[163] Y. Diao et al., J. Electrochem. Soc. 159 (2012) A1816–A1821.
[164] O. El Jaroudi et al., Inorg. Chem. 38 (1999) 2394–2401.
[165] G.J. Janz et al., Inorg. Chem. 15 (1976) 1755–1758.
[166] K.H. Wujcik et al., Adv. Energy Mater. 5 (2015) 1500285.
[167] D. Prendergast, G. Galli, Phys. Rev. Lett. 96 (2006) 215502.
[168] T.A. Pascal et al., PCCP 17 (2015) 7743–7753.
[169] T.A. Pascal et al., J. Phys. Chem. Lett. 5 (2014) 1547–1551.

Please cite this article in press as: X. Chen et al., Materials Today, (2018), https://doi.org/10.1016/j.mattod.2018.04.007

[170] M. Cuisinier et al., Adv. Energy Mater. 5 (2015) 1401801.
[171] K.H. Wujcik et al., J. Phys. Chem. C 120 (2016) 18403–18410.
[172] M. Cuisinier et al., Energy Environ. Sci. 7 (2014) 2697–2705.
[173] M. Cuisinier et al., J. Phys. Chem. Lett. 4 (2013) 3227–3232.
[174] J. Gao et al., J. Phys. Chem. C 115 (2011) 25132–25137.
[175] M.A. Lowe et al., RSC Adv. 4 (2014) 18347–18353.
[176] M.U. Patel et al., ChemPhysChem 15 (2014) 894–904.
[177] M. Vijayakumar et al., PCCP 16 (2014) 10923–10932.
[178] K.H. Wujcik et al., J. Electrochem. Soc. 161 (2014) A1100–A1106.
[179] T.Z. Hou et al., 2D Mater. 2 (2015) 014011.
[180] Y. Fu et al., Angew. Chem. Int. Ed. 52 (2013) 6930–6935.
[181] C. Jin et al., J. Mater. Chem. A 5 (2017) 632–640.
[182] F. Wu et al., J. Mater. Chem. A 2 (2014) 6064–6070.
[183] H. Kim et al., J. Power Sources 226 (2013) 256–265.
[184] G. Zheng et al., Nano Lett. 13 (2013) 1265–1270.
[185] Y. Li et al., RSC Adv. 5 (2015) 44160–44164.
[186] J. Liu et al., Nano Lett. 17 (2017) 5064–5070.
[187] X. Liu et al., Small 13 (2017) 1702104.
[188] F. Wu et al., Adv. Mater. 28 (2016) 6365–6371.
[189] H.J. Peng et al., Adv. Mater. 28 (2016) 9551–9558.
[190] H.J. Peng et al., Angew. Chem. Int. Ed. 55 (2016) 12990–12995.
[191] Y. Zhong et al., J. Phys. Chem. C 121 (2017) 14222–14227.
[192] Z. Li et al., Joule 1 (2017) 576–587.
[193] X. Tao et al., Nano Lett. 14 (2014) 5288–5294.
[194] L. Ma et al., ACS Nano 11 (2017) 7274–7283.
[195] F. Wu et al., Energy Environ. Sci. (2018), https://doi.org/10.1039/c8ee00419f.
[196] L. Ma et al., J. Mater. Chem. A 3 (2015) 19857–19866.
[197] Q. Pang et al., Mater. Horiz. 3 (2016) 130–136.
[198] Z. Yuan et al., Nano Lett. 16 (2016) 519–527.
[199] Z. Li et al., ACS Appl. Mater. Interfaces 9 (2017) 38477–38485.
[200] Z. Sun et al., Nat. Commun. 8 (2017) 14627.
[201] L. Ma et al., Nano Lett. 17 (2017) 7839–7846.
[202] Y. Zhong et al., Adv. Funct. Mater. 28 (2018) 1706391.
[203] C. Li et al., Nano Res. (2018), https://doi.org/10.1007/s12274-018-2017-9.
[204] W. Cai et al., Adv. Funct. Mater. 28 (2018) 1704865.
[205] R. Fang et al., Energy Storage Mater. 10 (2018) 56–61.
[206] J. Zhao et al., J. Mater. Chem. A 4 (2016) 6124–6130.
[207] Y. Qie et al., Carbon 129 (2018) 38–44.
[208] X. Liang et al., Adv. Mater. 29 (2017) 1603040.
[209] M. Zhang et al., Energy Storage Mater. 5 (2016) 223–229.
[210] P. Partovi-Azar et al., PCCP 17 (2015) 22009–22014.
[211] N.N. Rajput et al., Chem. Mater. 29 (2017) 3375–3379.
[212] F. Cordier et al., J. Magn. Reson. 140 (1999) 510–512.
[213] F.A. Soto et al., Chem. Mater. 27 (2015) 7990–8000.
[214] Q. Liu et al., ChemSusChem 10 (2017) 786–796.
[215] L.E. Camacho-Forero et al., J. Phys. Chem. C 119 (2015) 26828–26839.
[216] H. Kim et al., Adv. Energy Mater. 5 (2015) 01792.
[217] F. Wu et al., Adv. Mater. 27 (2015) 101–108.
[218] F. Wu et al., Nano Energy 40 (2017) 170–179.
[219] Y. Zhu et al., Adv. Sci. 4 (2017) 1600517.
[220] R. Zhang et al., Angew. Chem. Int. Ed. 56 (2017) 7764–7768.
[221] Y. Wang et al., J. Mater. Chem. A 5 (2017) 23434–23439.
[222] L. Liu et al., Joule 1 (2017) 563–575.
[223] D. Lin et al., Nat. Nanotechnol. 11 (2016) 626–632.
[224] R. Zhang et al., Joule 2 (2018), https://doi.org/10.1016/j.joule.2018.02.001.
[225] Y. Takahata, A.D.S. Marques, J. Electron Spectrosc. 178 (2010) 80–87.
[226] K. Artyushkova et al., Chem. Commun. 49 (2013) 2539–2541.
[227] G. Yang et al., J. Mater. Chem. A 3 (2015) 8865–8869.
[228] F. Besenbacher et al., Catal. Today 130 (2008) 86–96.
[229] F. Li, J. Zhao, ACS Appl. Mater. Interfaces 9 (2017) 42836–42844.
[230] Z. Liu et al., ACS Appl. Mater. Interfaces 8 (2016) 4700–4708.
[231] A.D. Becke, J. Chem. Phys. 98 (1993) 5648–5652.
[232] A.D. Becke, Phys. Rev. A 38 (1988) 3098.
[233] C. Lee et al., Phys. Rev. B 37 (1988) 785.
[234] F. Brockherde et al., Nat. Commun. 8 (2017) 872.
[235] Q. Wu et al., J. Chem. Phys. 131 (2009) 164112.
[236] M.J. Phipps et al., Chem. Soc. Rev. 44 (2015) 3177–3211.
[237] P.R. Horn et al., PCCP 18 (2016) 23067–23079.
[238] Y. Mao et al., PCCP 19 (2017) 5944–5958.
[239] A. Jain et al., APL Mater. 1 (2013) 011002.
[240] A.L. Ward et al., ACS Cent. Sci. 3 (2017) 399–406.
[241] S. Chakraborty et al., ACS Energy Lett. 2 (2017) 837–845.
[242] A. Shinde et al., ACS Energy Lett. 2 (2017) 2307–2312.
[243] S. Kim et al., Energy Environ. Sci. 10 (2017) 2201–2211.
[244] A. Pulido et al., Nature 543 (2017) 657–664.
[245] R. Xiao et al., Sci. Rep. 5 (2015) 14227.
[246] H.L. Chen et al., Chem. Mater. 24 (2012) 2009–2016.
[247] G. Hautier et al., J. Mater. Chem. 21 (2011) 17147–17153.
[248] H. Chen et al., J. Am. Chem. Soc. 134 (2012) 19619–19627.
[249] A.P. Bartók et al., Sci. Adv. 3 (2017) e1701816.
[250] Z. Zhou et al., ACS Cent. Sci. 3 (2017) 1337–1344.
[251] J.D. Evans, F.-X. Coudert, Chem. Mater. 29 (2017) 7833–7839.
[252] R. Jinnouchi, R. Asahi, J. Phys. Chem. Lett. 8 (2017) 4279–4283.
[253] N. Artrith et al., Phys. Rev. B 83 (2011) 153101.
[254] N. Artrith, J. Behler, Phys. Rev. B 85 (2012) 045439.
[255] N. Artrith, A. Urban, Comput. Mater. Sci. 114 (2016) 135–150.

Please cite this article in press as: X. Chen et al., Materials Today, (2018), https://doi.org/10.1016/j.mattod.2018.04.007